

1 Antarctic permafrost processes and antiphase dynamics of cold-based
2 glaciers in the McMurdo Dry Valleys inferred from ¹⁰Be and ²⁶Al
3 cosmogenic-nuclides ~~Antiphase dynamics between cold-based glaciers in~~
4 ~~the Antarctic Dry Valleys region and ice extent in the Ross Sea during MIS~~
5 ~~5~~

6 Jacob T.H. Anderson¹, Toshiyuki Fujioka², David Fink³, Alan J. Hidy⁴, Gary S. Wilson^{1,5},
7 Klaus Wilcken³, Andrey Abramov⁶, Nikita Demidov⁷

8 ¹Department of Marine Science, University of Otago, PO Box 56, Dunedin, New Zealand

9 ²Centro Nacional de Investigación sobre la Evolución Humana, Burgos 09002, Spain

10 ³Australian Nuclear Science & Technology Organisation, New Illawarra Road, Lucas Heights, NSW,
11 2234, Australia

12 ⁴Center for Accelerator Mass Spectrometry, Lawrence Livermore National Laboratory, Livermore CA
13 94550, USA

14 ⁵GNS Science, PO Box 30368, Lower Hutt 5040, Wellington, New Zealand

15 ⁶Institute of Physicochemical and Biological Problems of Soil Science, Pushchino, Russia

16 ⁷Arctic and Antarctic Research Institute, St. Petersburg, Russia

17 *Correspondence to:* Jacob T.H. Anderson (jacob.anderson@otago.ac.nz)

18 **Abstract**

19 ~~During the interglacial and interstadials of Marine Isotope Stage 5 (MIS 5e, 5c, 5a), outlet and alpine~~
20 ~~glaciers in the Dry Valleys region, Antarctica, appear to have advanced in response to increased~~
21 ~~precipitation from enhanced open ocean conditions in the Ross Sea. We provide further evidence of this~~
22 ~~antiphase behaviour through retreat of a peripheral lobe of Taylor Glacier in Pearse Valley, a region~~
23 ~~that was glaciated during MIS 5. We measured cosmogenic ¹⁰Be and ²⁶Al in three granite cobbles from~~
24 ~~thin, patchy drift (Taylor 2 Drift) in Pearse Valley to constrain the timing of retreat of Taylor Glacier.~~
25 ~~Assuming simple continuous exposure, our minimum, zero erosion, exposure ages suggest Taylor~~
26 ~~Glacier partially retreated from Pearse Valley no later than 65–74 ka. Timing of retreat after 65 ka and~~
27 ~~until the Last Glacial Maximum (LGM) when Taylor Glacier was at a minimum position, remains~~
28 ~~unresolved. The depositional history of permafrost sediments buried below Taylor 2 Drift in Pearse~~
29 ~~Valley was obtained from ¹⁰Be and ²⁶Al depth profiles to ~3 metres in permafrost in proximity to the~~
30 ~~cobble sampling sites. Soil and sediment mixing and associated permafrost processes are not widely~~

31 studied or understood in the McMurdo Dry Valleys of Antarctica. In this study, we investigate the
32 stability and depositional history of near-surface permafrost sediments to ~3 m depth in Pearse and
33 lower Wright valleys using measured cosmogenic ^{10}Be and ^{26}Al depth profiles. At Pearse Valley, we
34 estimate a minimum depositional age of ~74 ka for the active-layer and paleoactive-layer sediments
35 (<0.65 m). Combined dDepth profile modelling of ^{10}Be and ^{26}Al gives a depositional age for near-
36 surface (<1.65 m) permafrost at Pearse Valley of $180\text{-ka}^{+20} / \text{-40 ka}$, implying deposition of permafrost
37 sediments predate MIS 5 advances of Taylor Glacier. Depth profile modelling of deeper permafrost
38 sediments (>2.09 m) at Pearse Valley are thus inferred to have a indicates a depositional age of >180
39 ka. The cobble and permafrost ages reveal Taylor Glacier advances during MIS 5 were non-erosive or
40 mildly erosive, preserving the underlying permafrost sediments and peppering boulders and cobbles
41 upon an older, relict surface. Our results are consistent with U/Th ages from central Taylor Valley, and
42 suggest changes in moisture delivery over Taylor Dome during MIS 5e, 5c and 5a appear to be
43 associated with the extent of the Ross Ice Shelf and sea ice in the Ross Sea. During the interglacial and
44 interstadials of Marine Isotope Stage 5 (MIS 5e, 5c, 5a), outlet and alpine glaciers in the
45 Dry Valleys region, Antarctica, appear to have advanced in response to increased precipitation from
46 enhanced open ocean conditions in the Ross Sea. We provide further evidence of this antiphase
47 behaviour through retreat of a peripheral lobe of Taylor Glacier in Pearse Valley, a region that was
48 glaciated during MIS 5. We measured cosmogenic ^{10}Be and ^{26}Al in three granite cobbles from thin,
49 patchy drift (Taylor 2 Drift) in Pearse Valley to constrain the timing of retreat of Taylor Glacier.
50 Assuming simple continuous exposure, our minimum, zero erosion, exposure ages suggest Taylor
51 Glacier partially retreated from Pearse Valley no later than 65–74 ka. Timing of retreat after 65 ka and
52 until the Last Glacial Maximum (LGM) when Taylor Glacier was at a minimum position, remains
53 unresolved. The cobble and permafrost ages reveal Taylor Glacier advances during MIS 5 were non-
54 erosive or mildly erosive, preserving the underlying permafrost sediments and peppering boulders and
55 cobbles upon an older, relict surface. Our results are consistent with U/Th ages from central Taylor
56 Valley, and suggest changes in moisture delivery over Taylor Dome during MIS 5e, 5c and 5a appear
57 to be associated with the extent of the Ross Ice Shelf and sea ice in the Ross Sea. At a coastal, lower
58 elevation site in neighbouring lLower Wright Valley, ^{10}Be and ^{26}Al depth profiles from a second
59 permafrost core exhibit near-constant concentrations with depth, and indicate the sediments are either
60 vertically mixed after deposition, or are sufficiently young and post-depositional nuclide production is
61 negligible relative to inheritance. $^{26}\text{Al}/^{10}\text{Be}$ concentration ratios for both depth profiles range between
62 4.0 and 5.2 and are all lower than the nominal surface production rate ratio of 6.75, indicating that prior
63 to deposition, these sediments experienced a complex, yet similar, exposure-burial history. Assuming
64 a single cycle exposure-burial scenario, the observed $^{26}\text{Al}/^{10}\text{Be}$ ratios are equivalent to a total minimum
65 exposure-burial history of ~1.2 Ma.

66 In proximity to the depth profile core site, we measured cosmogenic ¹⁰Be and ²⁶Al in three granite
67 cobbles from thin, patchy drift (Taylor 2 Drift) in Pearse Valley to constrain the timing of retreat of
68 Taylor Glacier. Assuming simple continuous exposure, our minimum, zero erosion, exposure ages
69 suggest Taylor Glacier partially retreated from Pearse Valley no later than 65–74 ka. Timing of retreat
70 after 65 ka and until the Last Glacial Maximum (LGM) when Taylor Glacier was at a minimum position,
71 remains unresolved. The surface cobble ages and permafrost processes reveal Taylor Glacier advances
72 during MIS 5 were non-erosive or mildly erosive, preserving the underlying permafrost sediments and
73 peppering boulders and cobbles upon an older, relict surface. Our results are consistent with U/Th ages
74 from central Taylor Valley, and suggest changes in moisture delivery over Taylor Dome during MIS
75 5e, 5c and 5a appear to be associated with the extent of the Ross Ice Shelf and sea ice in the Ross Sea.
76 These data provide further evidence of antiphase behaviour through retreat of a peripheral lobe of
77 Taylor Glacier in Pearse Valley, a region that was glaciated during MIS 5. Our new data corroborates
78 antiphase behaviour between outlet and alpine glaciers in the Dry Valleys region and ice extent in the
79 Ross Sea. We suggest a causal relationship of cold-based glacier advance and retreat that is controlled
80 by an increase in moisture availability during retreat of sea ice and perhaps the Ross Ice Shelf, and
81 conversely, a decrease during times of sea ice and Ross Ice Shelf expansion in the Ross Sea.

82

83 **1 Introduction**

84

85 Permafrost (perennially frozen ground) in the McMurdo Dry Valleys, Antarctica, contains valuable
86 records of paleoenvironmental information, yet the stability of permafrost sediments, and the processes
87 that influence sediment transport, erosion and deposition in the McMurdo Dry Valleys are not well
88 understood. Previous studies investigating chronology and stability of glacial drift deposits, sediments
89 and permafrost in the McMurdo Dry Valleys and Transantarctic Mountains typically focused on high
90 elevation sites (e.g., Bergelin et al., 2022; Bibby et al., 2016; Morgan et al., 2011; 2010; Ng et al., 2005;
91 Schäfer et al., 2000; Sugden et al., 1995). The objective of these studies has largely been to constrain
92 the ages and / or erosion and sublimation rates of early Pleistocene, Pliocene, and Miocene landscapes.
93 There only appears to be one study investigating the age and stability of permafrost below 1000 m
94 elevation (Morgan et al., 2010). Yet, understanding the depositional environment and stability of
95 permafrost at low elevations is important for interpreting landscape evolution, geomorphic processes
96 and polar climate change on Earth, and as a terrestrial analogue for Mars (e.g., Marchant & Head, 2007).
97 Studies have also revealed permafrost contain frozen reservoirs of ice, greenhouse gases, ancient
98 bacteria, and viruses (Adriaenssens et al., 2017; Gilichinsky et al., 2007; Ruggiero et al., 2023). Future
99 thawing of low elevation environments, from increasing atmospheric temperatures, could increase

100 microbial activity and release previously frozen gases, and nutrients, leading to unprecedented changes
101 in hydrological, and biogeochemical cycles.

102 Permafrost usually contains an active, cryoturbated, mobile sediment layer, up to ~70 cm in depth.
103 Active-layer thickness, thawing, and permeability is modulated by seasonal variations. Permafrost
104 sediments are episodically covered by advancing and retreating ice (Atkins, 2013), which can further
105 complicate the interpretation of permafrost stability, sediment transport and mixing. In the McMurdo
106 Dry Valleys, there is currently no clear trend of increase or decrease in active-layer thickness between
107 2006 and 2019 (Hrbáček et al., 2023). The lack of understanding permafrost dynamics limits our ability
108 to reconstruct permafrost stability or evolution through time. Further research is needed to explore the
109 rates and mechanisms by which sediments are transported and mixed via aeolian, fluvial, and periglacial
110 processes.

112 Key components influencing permafrost processes and overlying geomorphic landforms are the
113 climatic conditions and extent of the Antarctic ice sheets. During Plio-Pleistocene warm intervals, the
114 West Antarctic Ice Sheet (WAIS), and marine-based sectors of the East Antarctic Ice Sheet (EAIS)
115 underwent extensive retreat (Naish et al., 2009; Pollard & DeConto, 2009; Cook et al., 2013; Blackburn
116 et al., 2020; Patterson et al., 2014). Warmer than present global temperatures and higher than present
117 sea levels are also observed in recent prominent interglacial periods, i.e., MIS 31 (~1.07 Ma), MIS 11
118 (~400 ka), and MIS 5e (130 - 115 ka) (Dutton et al., 2015; Naish et al., 2009; Pollard & DeConto,
119 2009). The extent of ice sheet retreat during these recent warm intervals varied significantly within
120 different drainage basins and through time. During the penultimate interglacial (MIS 5e), the average
121 global temperature was ~1–2°C warmer than pre-industrial (Fischer et al., 2018; Otto-Bliesner et al.,
122 2013), Antarctic temperatures were ~3–5°C warmer (Jouzel et al., 2007) and global mean sea levels
123 were ~6–9 metres higher than present (Dutton & Lambeck, 2012; Kopp et al., 2009). With a global
124 average temperature currently ~1.1°C warmer than pre-industrial levels, and predicted to be ≥1.5°C in
125 the coming decades (IPCC, 2021), interglacial conditions, such as during MIS 5, are an important
126 analogue for evaluating future ice sheet behaviour and global climate processes under future warming
127 scenarios.

128
129
130
131 ~~Ice sheet modelling during the Last Interglacial (MIS 5e, 130–115 ka), projected Antarctic ice loss~~
132 ~~contributed ~3.5–7.5 m GMSL (global mean sea level), primarily from WAIS retreat (DeConto &~~
133 ~~Pollard, 2016; DeConto et al., 2021; Golledge et al., 2021; Turney et al., 2020).~~ Simulated ice sheet
134 retreat during MIS 5e by Golledge et al. (2021) suggested ice loss in the Thwaites and Pine Island sector
135 of the WAIS, whereas the Ross Ice Shelf remained intact. Conversely~~In contrast~~, simulations by

136 DeConto & Pollard (2016), and Turney et al. (2020) suggested retreat of the Ross Ice Shelf, followed
137 by retreat of the WAIS interior.

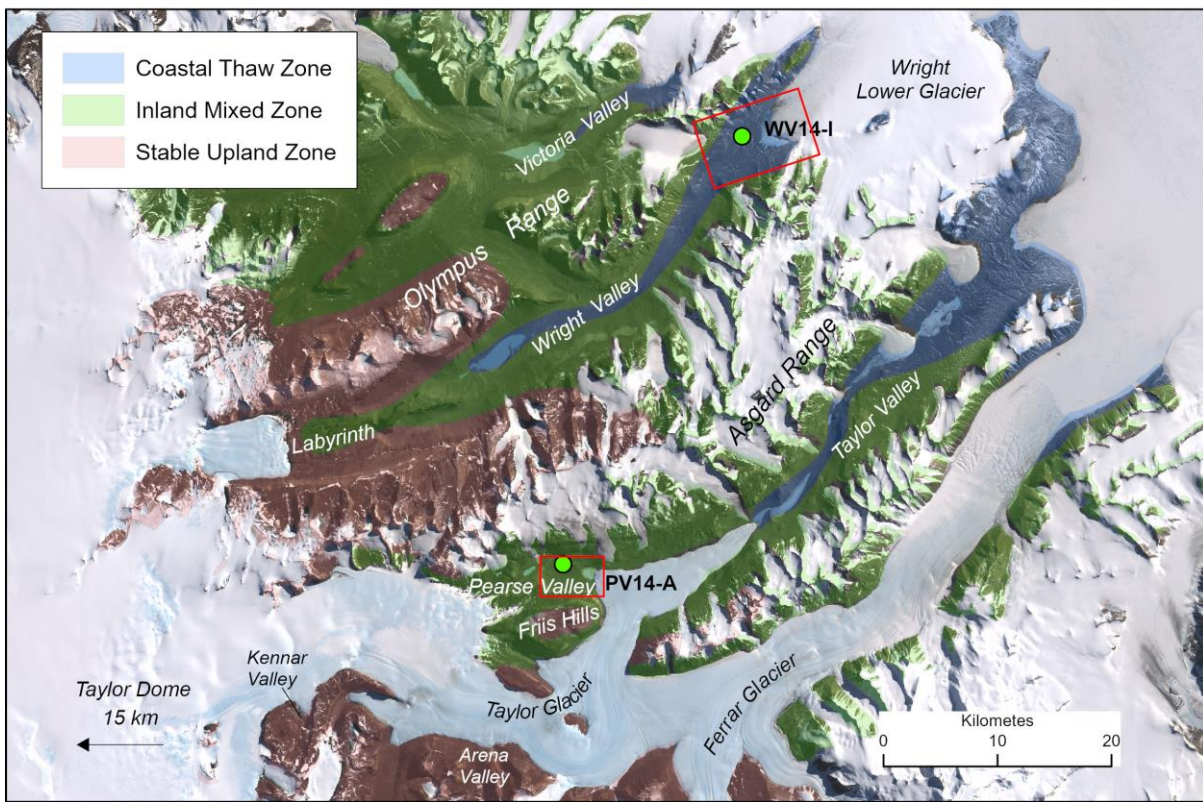
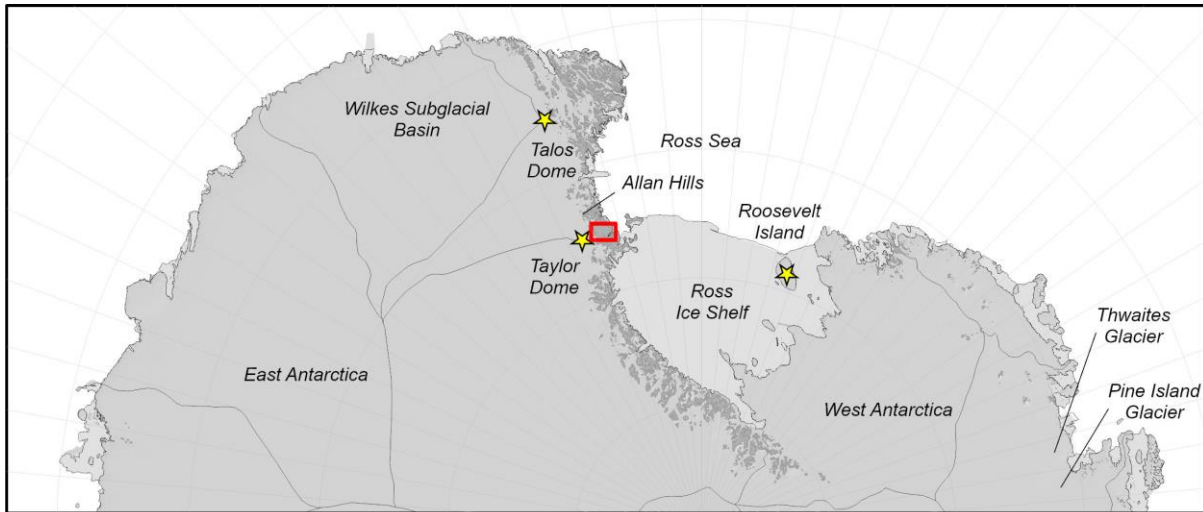
138
139 The $\delta^{18}\text{O}$ ice core records from Talos Dome reveal the EAIS was relatively intact during MIS 5 (Sutter
140 et al., 2020) and recent studies suggest partial ice sheet lowering in Wilkes Subglacial Basin but no
141 grounding line retreat (Fig. 1; Golledge et al., 2021; Sutter et al., 2020; Wilson et al., 2018). Ice core
142 studies reveal increased accumulation rates at Taylor Dome (Steig et al., 2000) and the Allan Hills Blue
143 Ice Area (Yan et al., 2021) near the onset of the Last Interglacial. Yan et al. (2021) hypothesized that
144 high accumulation rates during warm interglacials may reflect open ocean conditions in the Ross Sea,
145 caused by reduced sea ice extent, and possibly retreat of the Ross Ice Shelf relative to its present-day
146 position. This hypothesis is supported by a depleted $\delta^{18}\text{O}$ value (-0.175‰) from ice core records at
147 Roosevelt Island, indicating high sea level and reduced ice sheets during MIS 5a (Lee et al., 2020).

148
149 ~~In contrast,~~ terrestrial evidence from the McMurdo Dry Valleys suggests Taylor and Ferrar glaciers
150 were larger than present during ~~globally~~ warm interglacials of the mid-Pliocene climatic optimum (3.0–
151 3.1 Ma), MIS 31 (1.07 Ma) (Swanger et al., 2011) and MIS 5 (Brook et al., 1993; Higgins et al., 2000a).
152 ~~These~~ glacier advances appear to be out of phase with WAIS retreat and ocean warming during
153 interglacial periods. Alpine glaciers in the McMurdo Dry Valleys also appear out of phase with marine
154 based ice sheet retreat and advanced during MIS11 (Swanger et al., 2017), MIS 5 (Swanger et al., 2019),
155 and MIS 3 (Joy et al., 2017). ~~Glacial deposits and moraines, which can be used to reconstruct past ice~~
156 ~~extent, have been preserved where cold-based glaciers have advanced and retreated during Quaternary~~
157 ~~glaciations.~~ The past ice volume and extent of Taylor Glacier (during interglacial periods) has been
158 derived from cosmogenic nuclide studies and mapping drift and moraine deposits in lower Kennar
159 Valley (Swanger et al., 2011), and lower Arena Valley (Brook et al., 1993; Marchant et al., 1994), and
160 U/Th dating in central Taylor Valley (Higgins et al., 2000a). MIS 5 age glacial deposits in central Taylor
161 Valley and Arena Valley are mapped as Taylor 2 Drift (Bockheim et al., 2008; Brook et al., 1993; Cox
162 et al., 2012; Denton et al., 1970), termed Bonney Drift by Higgins et al. (2000b). By inference, glacial
163 deposits on the valley floor of Pearse Valley are mapped as Taylor 2 Drift (Bockheim et al., 2008; Cox
164 et al., 2012; Denton et al., 1970). U/Th ages of algal carbonates in central Taylor Valley suggest
165 multiple advance / retreat cycles of the Taylor Glacier snout during MIS 5, with retreat of Taylor
166 Glacier continuing after the MIS 5/4 transition (Higgins et al., 2000a). The $\delta^{18}\text{O}$ values measured from
167 buried ice in northern Pearse Valley also support the advance of Taylor Glacier during MIS 5 (Swanger
168 et al., 2019). However, the timing of advance and retreat of Taylor Glacier in central Taylor Valley and
169 in Pearse Valley remain poorly constrained.

170 ~~Previous studies investigating chronology and stability of glacial drift deposits, sediments and~~
171 ~~permafrost in the Dry Valleys and Transantarctic Mountains typically focused on high elevation sites~~

172 (~~e.g., Bergelin et al., 2022; Bibby et al., 2016; Morgan et al., 2011, 2010; Ng et al., 2005; Schäfer et al.,~~
173 ~~2000; Sugden et al., 1995~~). The objective of these studies has largely been to constrain the ages and/
174 ~~or erosion and sublimation rates of early Pleistocene, Pliocene, and Miocene landscapes. There only~~
175 ~~appears to be one study investigating the age and stability of permafrost below 1000 m elevation~~
176 ~~(Morgan et al., 2010). Yet, understanding the depositional environment and stability of permafrost at~~
177 ~~low elevations is important for interpreting landscape evolution, geomorphic processes and polar~~
178 ~~climate change on Earth, and as a terrestrial analogue for Mars (e.g., Marchant & Head, 2007).~~

179 In this study, we investigate the stability and depositional history of near-surface permafrost sediments
180 using paired ^{10}Be and ^{26}Al depth profiles of permafrost from Pearse and lower Wright valleys. We
181 compare the exposure-burial history of the permafrost cores from the two sites and the long-term
182 recycling processes of McMurdo Dry Valleys sediments. Here, we~~we also~~ investigate the relationship
183 between thin, patchy drift overlying permafrost sediments in Pearse Valley. Thin, patchy drift is the
184 only evidence of cold-based glacier overriding, and is defined as a scattering of clasts overlying older,
185 undisturbed desert pavements (Atkins, 2013). We present cosmogenic nuclide surface exposure ages
186 from three cobbles in Pearse Valley to determine the age of Taylor 2 Drift, and provide constraints on
187 the timing of retreat of a peripheral lobe of Taylor Glacier during MIS 5. ~~To determine the relationship~~
188 ~~between the thin, patchy drift and underlying permafrost sediments at Pearse Valley, we also present~~
189 ~~companion ^{10}Be and ^{26}Al depth profiles of permafrost.~~ Combining permafrost depth profiles and
190 exposure ages of cobbles from the drift ~~and permafrost depth profiles~~, we ~~constrain a minimum age of~~
191 ~~Taylor Glacier retreat, and~~ infer the depositional history of the permafrost sediments and constrain a
192 minimum age of Taylor Glacier retreat. These data from Pearse Valley provide insight into Taylor
193 Glacier behaviour and associated geomorphic processes during MIS 5. ~~Additionally, we present ^{10}Be~~
194 ~~and ^{26}Al permafrost depth profiles from a coastal, lower elevation site in the neighbouring Lower Wright~~
195 ~~Valley, and together with the Pearse Valley depth profiles, discuss long term recycling processes of~~
196 ~~Dry Valleys sediments.~~



197

198 **Figure 1.** Study area and location of McMurdo Dry Valleys. Yellow stars show ice core sites discussed
 199 in the text. The green circles show the locations of the Pearse Valley and Lower Wright Valley sites
 200 where permafrost cores were recovered. The three microclimatic zones are the stable upland zone
 201 (brown), inland mixed zone (green), and coastal thaw zone (blue). Modified from Marchant and Head
 202 (2007); and Salvatore and Levy, (2021). Red rectangles in the lower diagram show the locations of
 203 Pearse Valley in Fig. 2 and Lower Wright Valley in Fig. 3.

204

205

206 **2 Geologic setting and study area**

207 The Dry Valleys are a hyperarid, cold polar desert and can be subdivided into three geographic zones
208 (stable upland, inland mixed, and coastal thaw zones), which are defined by their microclimatic
209 parameters of atmospheric temperature, soil moisture, and relative humidity (Fig. 1; Marchant &
210 Denton, 1996; Marchant & Head, 2007). The stability and evolution of geomorphic features and
211 permafrost are controlled by subtle variations within each microclimatic zone. The active-layer in
212 permafrost is defined as soil horizons where the ground temperature fluctuates above and below 0°C
213 seasonally (Davis, 2001; Yershov, 1998). Antarctic permafrost soils along the floors and flanks of ice-
214 free valleys are vertically mixed, initially through deposition of reworked sediments, and secondarily
215 through active-layer cryoturbation up to 70 cm depth of the surface (Bockheim et al., 2007; 2008).
216 Cryoturbation is defined as soil movement due to repeated freeze–thaw, generally within the active-
217 layer of permafrost (French, 2017). Active-layers can be distinguished by the presence (wet active-
218 layer) or absence (dry active-layer) of water. Soils in the coastal thaw zone are seasonally moist and
219 comprise wet active-layers, whereas soils in the inland mixed zone are dry and comprise dry active-
220 layers (Marchant & Head, 2007). Our study sites focused on two different microclimatic zones (Fig. 1);
221 Pearse Valley in the inland mixed zone, and Lower Wright Valley in the coastal thaw zone, which
222 differ in age, elevation, and distance from the coast.

223 **2.1 Pearse Valley**

224 Pearse Valley is an ice-free valley that is bounded by the Friis Hills in the south, the Asgard Range in
225 the north and opens onto peripheral lobes of Taylor Glacier in the east and west (Fig. 1). Taylor Glacier
226 flows east from Taylor Dome of the EAIS, terminating in Taylor Valley. At the eastern end of Pearse
227 Valley, a lobe of Taylor Glacier terminates into Lake Joyce, a closed-basin proglacial lake (Fig. 2).
228 Taylor Glacier and local alpine glaciers have advanced in the present interglacial and occupy their
229 maximum position since the Last Glacial Maximum (LGM) (Higgins et al., 2000a). At the head of
230 Pearse Valley, glacially incised bedrock sits at a similar elevation to the Labyrinth platform in upper
231 Wright Valley, likely formed by a network of subglacial drainage channels beneath wet-based glacial
232 conditions during the Miocene Climate Transition (Fig. 1; Lewis & Ashworth, 2016; Chorley et al.,
233 2022). The northern valley wall comprises gelifluction lobes, buried snowpack deposits, meltwater
234 channels derived from ephemeral streams, and fans fed by the meltwater channels in front of the lobes
235 (Heldmann et al., 2012; Swanger et al., 2019). The valley floor consists of a lower elevation area on the
236 southern side, and a higher elevation area on the northern side of the valley. The PV14-A core and
237 cobble samples are located on the central northern side of the valley floor (Fig. 2).

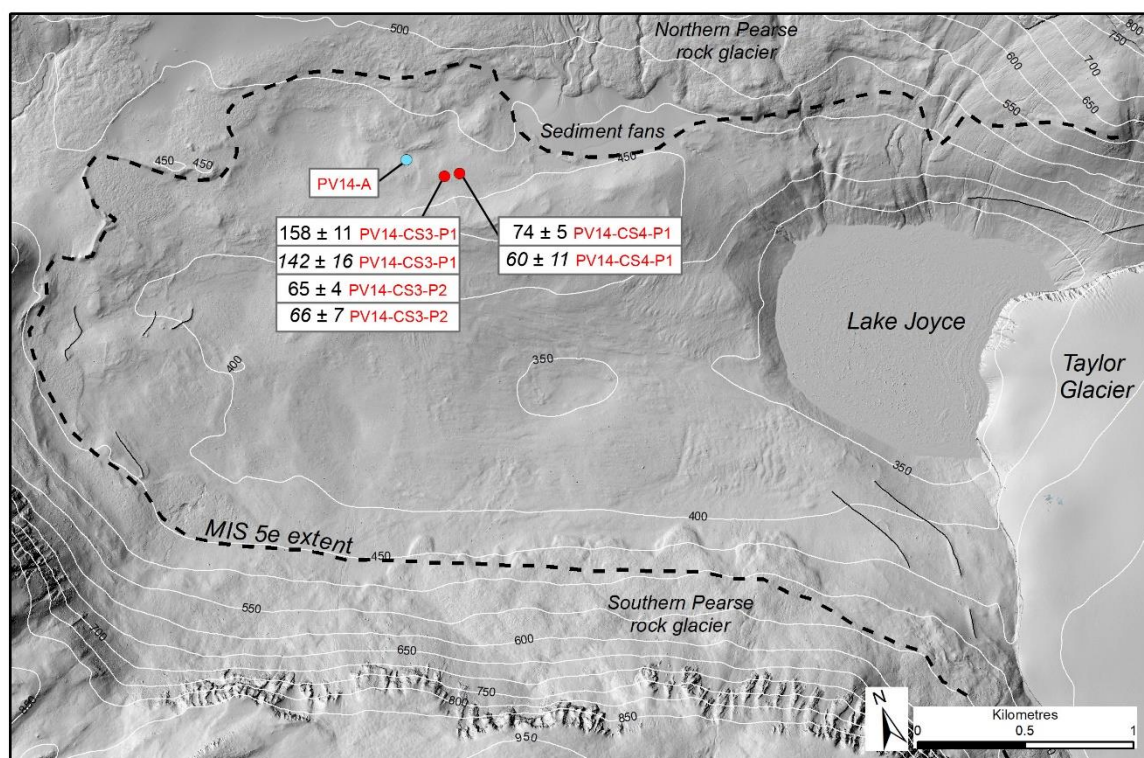
238 The local bedrock comprises basement granites and Ferrar dolerite intrusives (Cox et al., 2012; Gunn &
239 Warren, 1962). Glacial deposits on the valley floor are mapped as Taylor 2 Drift (Bockheim et al., 2008;
240 Denton et al., 1970). These sediments were inferred as waterlain and melt-out tills following the
241 penultimate down-valley advance of the Taylor Glacier during MIS 5 (70 – 130 ka) (Cox et al., 2012;

242 Higgins et al., 2000a; Swanger et al., 2019). The valley floor landscape is characterized by hummocky
243 moraines with a combination of glacial, and fluvial deposits, and aeolian sediments. Variably
244 weathered granite boulders (up to 3 m in diameter) form a lag deposit on the drift surface, inferred as a
245 till deflation or a separate younger depositional unit (Higgins et al., 2000b). The northern and southern
246 Pearse Valley walls comprises extensive rock glaciers (Swanger et al., 2019).

247

248 2.1.1 Modern climate

249 Pearse Valley is situated in the inland mixed zone of the Dry Valleys (Marchant & Denton, 1996). The
250 valley has a mean annual temperature of -18°C (Marchant et al., 2013) and precipitation rates of 20–50
251 mm/yr (water equivalent), and 100–200 mm/yr in the adjacent Asgard Range, the source region for the
252 local alpine glaciers (Fountain et al., 2010). Mean summer air temperatures (December through
253 February) in Pearse Valley are -2 to -7°C (Marchant et al., 2013). Ground surface temperatures measured
254 at the Pearse Valley meteorological station between 27–28 November, 2009, recorded a peak
255 temperature of 10°C due to solar heating (Heldmann et al., 2012). Winds in Pearse Valley are strong
256 enough to mobilise sand grains and form aeolian surface features such as sand dunes (Heldmann et al.,
257 2012).



258

259 **Figure 2.** Map of Pearse Valley with MIS 5e extent of Taylor Glacier (black dashed line; Cox et al.,
260 2012), sample locations and PV14-A permafrost drill site (blue circle). Thin black lines trace undated
261 moraines. PV14-A drill site (blue circle) and measured ^{10}Be and ^{26}Al (italics) ages of cobbles residing

262 on boulders are shown in kiloyears with 1σ uncertainties (red circles). Lidar image from Fountain et al.
263 (2017).

264

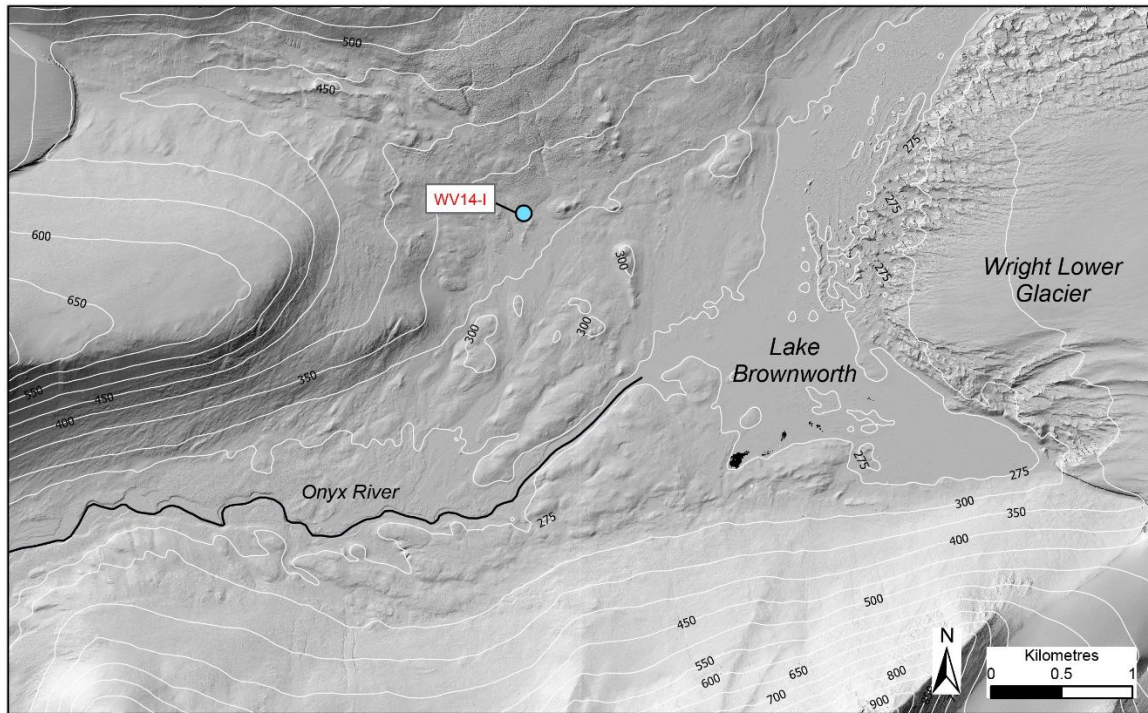
265 **2.2 Lower Wright Valley**

266 Lower Wright Valley is ice-free and is bounded by the Asgard Range in the south, and the Olympus
267 Range in the north (Fig. 1). The mouth of the valley at the eastern end is cut off from the Ross Sea by
268 the Wright Lower Glacier, a lobe of the Wilson Piedmont Glacier. Lake Brownworth, a proglacial lake
269 fed by the Wright Lower Glacier, supplies the westward flowing Onyx River. The WV14-I core is
270 located on the northern side of **L**ower Wright Valley (Fig. 3). Radiocarbon dates of lacustrine algae
271 from glaciolacustrine deposits suggest Lake Brownworth is a small remnant of a much larger lake that
272 existed during the LGM and early Holocene (Hall et al., 2001). The post-glacial, Holocene age
273 landscapes form hummocky moraines, with a combination of deltas, shorelines and glaciolacustrine
274 sediments (Hall et al., 2001). Glacial meltwater streams drain into Lake Brownworth and the Onyx
275 River from the north and south valley walls. The local bedrock comprises basement metasediments and
276 granites, and Ferrar dolerite intrusives (Cox et al., 2012). Metasediments, granite, dolerite and
277 occasional basalt sediments in the **L**ower Wright Valley have accumulated since the last deglaciation
278 by lacustrine, fluvial and aeolian processes (Hall et al., 2001; Hall & Denton, 2005).

279

280 **2.2.1 Modern climate**

281 Lower Wright Valley is situated in the coastal thaw zone of the **McMurdo** Dry Valleys (Marchant &
282 Denton, 1996) and has a mean annual temperature of -21°C (Doran et al., 2002) and precipitation rates
283 of 26–51 mm/yr (water equivalent) (Fountain et al., 2010). Mean summer air temperatures (December
284 through February) in **L**ower Wright Valley are -5 to -7°C , and can exceed 0°C for >6 days per year
285 (Doran et al., 2002). Meltwater forms during summer months (December and January) when
286 temperatures can rise to as much as 10°C at some locations (Hall et al., 2001).



287

288 **Figure 3.** Map of Lower Wright Valley and WV14-I permafrost drill site (blue circle). Lidar image
 289 from Fountain et al. (2017).

290

291 3 Methods

292 3.1 Surface exposure sample collection

293 ~~Three granite cobble samples were collected for surface exposure analysis from Pearse Valley (Table~~
 294 ~~1; Fig. 2). We targeted perched cobbles, resting on larger flat boulders to minimise the possibility of~~
 295 ~~post depositional disturbance and hence best reflect deposition from retreating glacier ice or from~~
 296 ~~surface deflation through sublimation. Samples that showed minimal weathering or fracturing were~~
 297 ~~selected. The three cobbles were perched on larger host boulders (>1 m diameter) which were elevated~~
 298 ~~above the local surface permafrost valley deposits (Fig. 4). Two samples (PV14 CS3 P1 and PV14-~~
 299 ~~CS3 P2) are small cobbles perched on the same host boulder, while the third sample (PV14 CS4 P1) is~~
 300 ~~a slightly larger cobble perched on a different host boulder less than 80 metres away.~~

301

302 ~~**Figure 4.** Boulders and cobbles from Taylor 2 Drift on the central northern side of Pearse Valley. (a)~~
 303 ~~PV14 CS3 P1 and PV14 CS3 P2 cobbles perched on a dolerite boulder. (b) Close view of PV14 CS3-~~
 304 ~~P2. (c) PV14 CS4 P1 cobble hosted on dolerite boulder. (d) A granite boulder, hosting a dolerite~~
 305 ~~boulder.~~

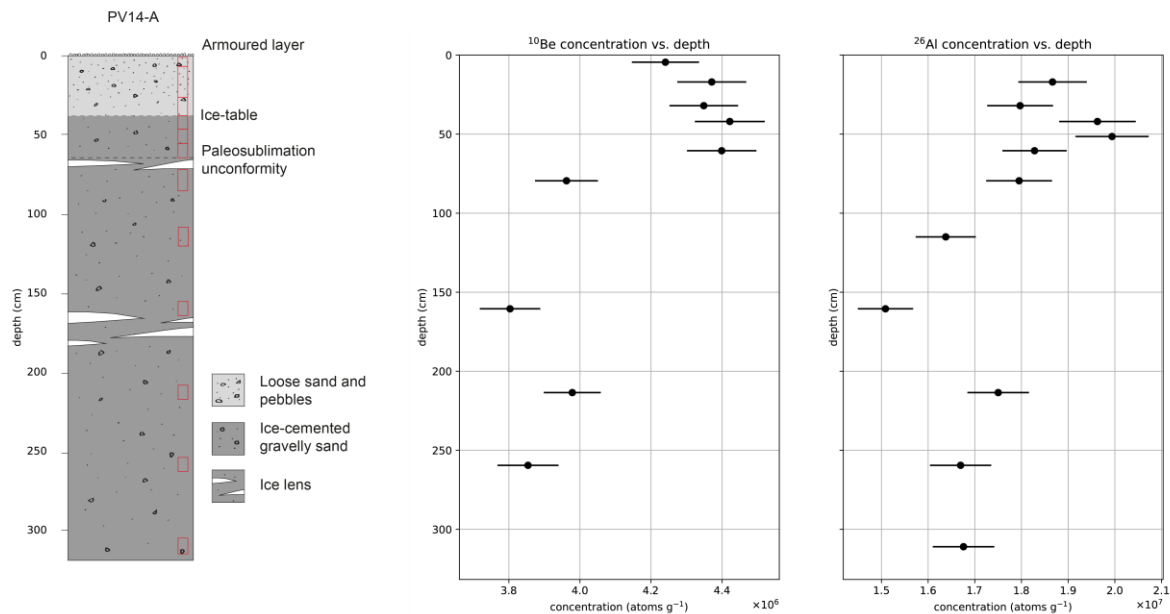
306

3.12 Permafrost core locations and characteristics

During the 2014/15 austral field season, permafrost cores were recovered from Pearse Valley and Lower Wright Valley using a gasoline powered dry drilling technique (Fig. 1). These two cores were sampled for sedimentological and for cosmogenic nuclide analysis. After extraction, the core sections were divided into ~10 cm portions for sub-sampling and analysis. ~~Permafrost sediments were collected in a combination of Whirl Pak bags and PVC core liners. The upper sections were collected in Whirl Pak bags as the core recovery was poor. Core integrity below the active-layer in ice-cemented permafrost sediments was good and cores were collected as rigid intact sections in PVC core liners.~~

3.12.1 Pearse Valley borehole core

The PV14-A core is located on an elevated bench that extends along the northern side of the valley floor at 450 masl (77.7062°S, 161.5467°E), ~3 km north-west of the present position of the Taylor Glacier lobe (Fig. 2). The core was recovered to a depth of 3.16 m (Fig 45a; Table 2). The active-layer (0 – 0.37 m) above the ice-cemented permafrost consists of a thin armoured surface layer of desert pavement (~0.02 m thick), ~~and which caps~~ a layer of loose dry sand (~0.35 m thick). Recovered sediments from beneath the armoured desert pavement comprise a dry active-layer of loose sand and pebbles down to 0.37 m depth. Below 0.37 m depth, the recovered sediments comprise ice-cemented permafrost, ~~with grains of sand and pebbles forming the matrix, and the pore spaces filled with ice.~~ The ¹⁰Be and ²⁶Al depth profiles (Fig. 4) start below the 0.02 m thick surface armoured pavement. The first three samples were collected from the dry active-layer ~~followed by~~ and nine from the ice-cemented permafrost ~~(Fig. 5a)~~. Sediments within the permafrost core comprise gravelly sands derived from weathered Beacon Supergroup, granite, granodiorite, diorite, and dolerite origins, ~~which are~~ They appear structureless, or weakly bedded, ~~which we interpret to be fluvio-glacial and aeolian deposits.~~ Between 0.73–0.86 m depth, the core comprises several ice lenses indicative of ice accumulation below a paleosublimation unconformity. Several small ice lenses were also recovered between 1.57–1.87 m depth. ~~The ice lenses are typically clean ice or debris-poor ice compared to adjacent upper and lower segments.~~ Only two of the three active-layer samples, and six of the nine permafrost core samples were successful in providing paired ¹⁰Be and ²⁶Al concentrations (Fig. 4; Table 1).



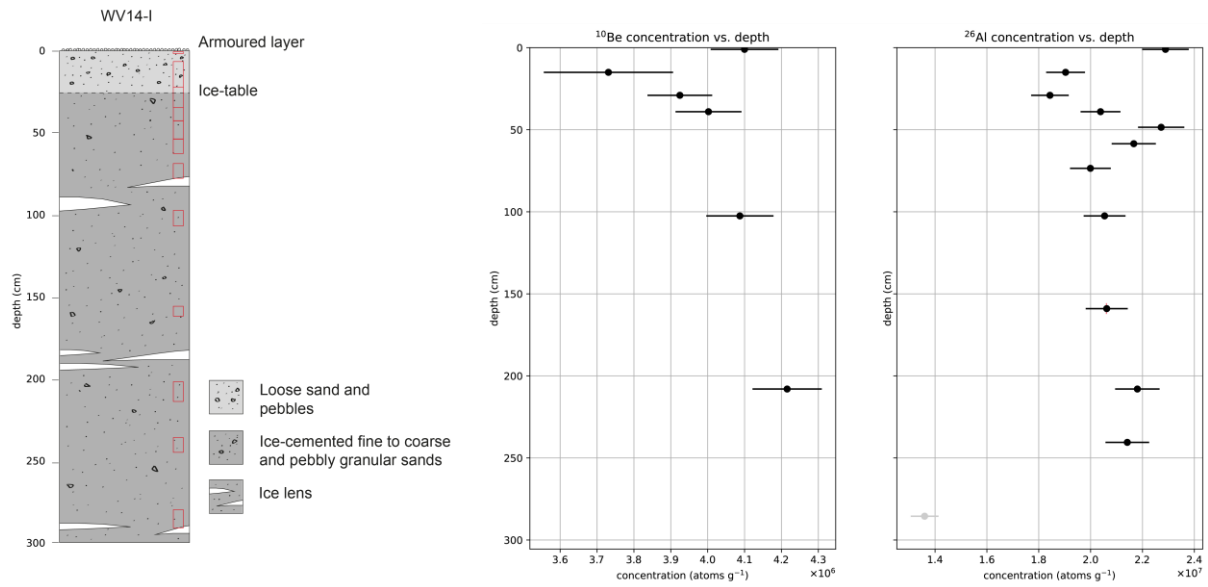
335

336 **Figure 4.** Pearse Valley (PV14-A) permafrost core sedimentology (left). Locations of cosmogenic
 337 nuclide samples shown in red boxes. The modern active-layer is from 0–0.37 m depth. Pearse Valley
 338 (PV14-A) permafrost core depth profiles with measured ^{10}Be and ^{26}Al concentrations (black data points)
 339 with 1σ uncertainties (right). For all samples between 0.02–0.65 m depth, we used the average
 340 concentration of all five ^{10}Be and ^{26}Al measurements to represent the effect of cryoturbation of
 341 sediments in the active- and paleoactive-layer (see text). Note the rise in ^{10}Be and ^{26}Al concentrations
 342 below 2.09 m.

343

344 3.12.2 Lower Wright Valley borehole core

345 The WV14-I core is located in eastern Wright Valley at 326 masl (77.4252°S, 162.6664°E), ~2 km west
 346 of Wright Lower Glacier (Fig. 3). The core was recovered to a depth of 2.91 m (Fig. 5b; Table 2). The
 347 active-layer (0–0.28 m) above the ice-cemented permafrost consists of a thin armoured surface layer of
 348 desert pavement (~0.02 m thick), ~~which caps~~ a layer of loose sand and pebbles (~0.26 m thick).
 349 Below 0.28 m depth, the recovered sediments comprised ice-cemented permafrost. The ^{10}Be and ^{26}Al
 350 depth profiles start on the armoured desert pavement. Two samples were collected from the active-layer
 351 and 10 from the ice-cemented permafrost (Fig. 5b). The permafrost sediments are structureless, to thinly
 352 laminated, fine to coarse, and pebbly granular sands, which we interpret to be fluvial and aeolian
 353 deposits. Sediments within the core are derived from weathered granite, metasedimentary, dolerite and
 354 basalt origins. From 0–0.98 m depth, core sections were broken and loose sediment was recovered.
 355 Sediments recovered from 0.98–2.91 m were ice-cemented, except when encountering ice lenses.
 356 Several small ice lenses were recovered between 1.80–2.03 m depth. Hall et al. (2001) suggested
 357 sediments at Lower Wright Valley are delta, shoreline and glaciolacustrine deposits associated with a
 358 large proglacial lake at the LGM and in the early Holocene (25–7 ka). Only four of the 10 permafrost
 359 core samples were successful in providing paired ^{10}Be and ^{26}Al concentrations (Fig 5; Table 1).



360

361 **Figure 5.** Lower Wright Valley (WV14-I) permafrost core sedimentology (left). Locations of
 362 cosmogenic nuclide samples shown in red boxes. The modern active-layer is from 0–0.28 m depth.
 363 lower Wright Valley (WV14-I) permafrost core depth profiles with measured ^{10}Be and ^{26}Al
 364 concentrations (black data points) with 1σ uncertainties (right).

365

366 **3.2 Surface cobbles at Pearse Valley**

367 Three granite cobble samples were collected for surface exposure analysis from Pearse Valley (Table
 368 2; Fig. 2). We targeted perched cobbles, resting on larger flat boulders to minimise the possibility of
 369 post-depositional disturbance and hence best reflect deposition from retreating glacier ice or from
 370 surface deflation through sublimation. Samples that showed minimal weathering or fracturing were
 371 selected. The three cobbles were perched on larger host boulders (>1 m diameter) which were elevated
 372 above the local surface permafrost valley deposits (Fig. 6). Two samples (PV14-CS3-P1 and PV14-
 373 CS3-P2) are small cobbles perched on the same host boulder, while the third sample (PV14-CS4-P1) is
 374 a slightly larger cobble perched on a different host boulder less than 80 metres away.



375

376 **Figure 6.** Boulders and cobbles from Taylor 2 Drift on the central northern side of Pearse Valley. (a)
 377 PV14-CS3-P1 and PV14-CS3-P2 cobbles perched on a dolerite boulder. (b) Close view of PV14-CS3-
 378 P2. (c) PV14-CS4-P1 cobble hosted on dolerite boulder. (d) A granite boulder, hosting a dolerite
 379 boulder.

380

381

382 3.3 Analytical methods

383 Each core sample processed for cosmogenic nuclide analysis was heated at 100°C overnight to remove
 384 ice and dry the sediment. Dried core samples, and cobble surface samples were crushed and sieved to
 385 obtain the 250 – 500 µm fraction. Quartz was separated and purified using the hot phosphoric acid
 386 method (Mifsud et al., 2013) and beryllium and aluminium were extracted from quartz via conventional
 387 HF dissolution and ion exchange chromatography (Child et al., 2000). Isotope ratios were measured by
 388 Accelerator Mass Spectrometry on the SIRIUS accelerator at the Australian Nuclear Science and
 389 Technology Organisation (Wilcken et al., 2019).

390 Measured $^{10}\text{Be}/^9\text{Be}$ ratios were normalised to the 07KNSTD (KN-5.2) standard of Nishiizumi et al.
 391 (2007) with a nominal $^{10}\text{Be}/^9\text{Be}$ ratio of 8560×10^{-15} . Measured $^{26}\text{Al}/^{27}\text{Al}$ ratios were normalised to the
 392 KNSTD (KN-4.2) standard of Nishiizumi (2004) with a nominal $^{26}\text{Al}/^{27}\text{Al}$ ratio of 30960×10^{-15} . The

393 nuclide concentration data for the Pearse Valley and lower Wright Valley depth profiles, and perched
394 cobbles from Pearse Valley, and Pearse Valley and Lower Wright Valley depth profiles are shown in
395 Tables 1 and 2, respectively. Full procedural $^{10}\text{Be}/^9\text{Be}$ blanks were obtained using a carrier solutions
396 derived/processed from dissolved beryl mineral with a known ^9Be concentrations (1068 and 1048 $\mu\text{g/g}$
397 (solution)) and resulted in ratios of $1.9 \pm 0.4 \times 10^{-15}$ and $1.3 \pm 0.3 \times 10^{-14}$. Blank corrections to measured
398 $^{10}\text{Be}/^9\text{Be}$ ratios amounted to $<2\%$. Procedural $^{26}\text{Al}/^{27}\text{Al}$ blanks were processed from standard reference
399 ICP aluminium solutions (1000 $\mu\text{g/ml} \pm 1\%$) and resulted in ratios $3.6 \pm 1.7 \times 10^{-14}$ and $1.3 \pm 0.6 \times 10^{-15}$.
400 Blank corrections to measured $^{26}\text{Al}/^{27}\text{Al}$ ratios amounted to 4% to 35% for Pearse Valley erratics and
401 $<1\%$ for all other samples. Final errors in ^{10}Be and ^{26}Al concentrations are obtained by quadrature
402 addition of the final AMS analytical error (the larger of the total statistical or standard mean error), a
403 reproducibility error based on the standard deviation of the set of standard reference samples measured
404 during the run (typically 1-2% for either ^{10}Be or ^{26}Al), a 1% error in Be spike concentration and a
405 representative 3% error for ICP Al concentration of the native ^{27}Al in the final purified quartz powder.
406 Unless otherwise stated, all analytical uncertainties are 1σ .

407 Surface exposure ages for the cobble samples were calculated using version 3 of the CRONUS-Earth
408 calculator (<http://hess.ess.washington.edu/>; Balco et al., 2008) using the LSDn scaling scheme (Lifton et
409 al., 2014) and the primary default calibration data set of Borchers et al. (2016) (Table 1). Complete
410 analytical data for all measurements are shown in Table S1, and data from surface samples are archived
411 on the ICE-D Antarctica database (<http://antarctica.ice-d.org>).

412

413 **3.4 Dual nuclide depth profile models and parameters**

414 ^{10}Be and ^{26}Al data from core samples at Pearse and lower Wright valleys were modelled as simple
415 exposure depth profiles used to model the surface exposure age of permafrost sediments at Pearse and
416 Lower Wright valleys via the depth profile technique (sensu Anderson et al., 1996). From a process
417 perspective this assumes that (1) the modelled sediment package is vertically well-mixed at the time of
418 deposition such that inherited nuclide concentration is constant with depth; (2) post-depositional
419 sediment mixing is absent and changes in bulk density do not occur over time; and (3) surface erosion is
420 steady-state. While the sedimentology of the cores clearly indicates that these assumptions were not fully
421 realised, this simplified model provides a useful tool for exploring the impact of various soil and
422 permafrost processes while providing useful chronologic constraints. We implemented a modified
423 version of the Monte Carlo-based code of Hidy et al. (2010) that allows profiles of both ^{10}Be and ^{26}Al to
424 be modelled jointly (after Hidy et al. (2018)). For shallow profiles in sediments, where non-unique
425 solutions for exposure age and erosion rate are likely, this approach allows estimation of exposure age
426 and pre-depositional nuclide concentration (i.e., inheritance) given reasonable observation-based

427 constraint on erosion rate or net erosion (e.g., Bergelin et al., 2022; Hidy et al., 2010, 2018; Mercader et
428 al., 2012; Morgan et al., 2010).

429 ~~The simplest assumptions are that all depth profile sediments have the same inherited nuclide~~
430 ~~concentration at the time of deposition and that post-depositional sediment mixing is absent. The~~
431 ~~inheritance determined by the best-fit depth profile asymptote can be subtracted from the measured~~
432 ~~values for each sample (Hidy et al., 2018). The former is a reasonable assumption for our core samples~~
433 ~~given that these sediments comprise a combination of well mixed, thick glacial tills, fluvial and aeolian~~
434 ~~sediments that were deposited at a given time when the ice retreated from each valley.~~ As described in
435 Sect. 3.12 above, the upper ~0.3 m of both cores consists of loose sandy sediment that is mobile or active.
436 Fig. 76 shows a schematic the evolution of a cosmogenic nuclide depth profile over time with the added
437 feature of a near-constant ^{10}Be concentration in a cryoturbated active-layer above ice-cemented
438 permafrost sediments. ~~The presence of a surface mixed-layer does not negate the assumption that these~~
439 ~~sediments were comprised of a combination of well mixed, thick glacial tills, fluvial, and aeolian~~
440 ~~sediments that were deposited at a given time when the glaciers retreated from each valley. However,~~
441 ~~consideration needs to be given on how to represent the measured ^{10}Be and ^{26}Al concentrations in the~~
442 ~~surface mixed-layer with the depth profiles and resultant sensitivity of the model outputs. We discuss~~
443 ~~these aspects in Sect. 4 below.~~

444 ~~Any post-depositional nuclide production is unknown, but the inheritance determined by the best-fit depth profile~~
445 ~~asymptote can be subtracted from the measured values for each sample (Hidy et al., 2018).~~

446 To ensure consistency with the cobble exposure ages, we obtain production rates applied in the depth
447 profile model from the CRONUS-Earth calculator. For the PV14-A core, we use a site-specific spallation
448 ^{10}Be surface production rate of $8.40 \text{ atoms-}^{10}\text{Be g}^{-1} (\text{quartz}) \text{ yr}^{-1}$, and a ^{26}Al surface production rate of
449 $59.7 \text{ atoms-}^{26}\text{Al g}^{-1} (\text{quartz}) \text{ yr}^{-1}$. For the WV14-I core, we use a site-specific spallation ^{10}Be surface
450 production rate of $7.47 \text{ atoms-}^{10}\text{Be g}^{-1} (\text{quartz}) \text{ yr}^{-1}$, and a ^{26}Al surface production rate of $53.2 \text{ atoms-}^{26}\text{Al}$
451 $\text{g}^{-1} (\text{quartz}) \text{ yr}^{-1}$. These production rates were calculated using LSDn scaling (Lifton et al., 2014) and the
452 primary calibration data set of Borchers et al. (2016). These production rates yield $^{26}\text{Al}/^{10}\text{Be}$ surface
453 production rate ratios of 7.11 and 7.12 for Pearse Valley and Lower Wright Valley, respectively. We
454 assume a neutron attenuation length of $140 \pm 5 \text{ g cm}^{-2}$, as used in previous Antarctic studies for ^{10}Be and
455 ^{26}Al (Bergelin et al., 2022; Borchers et al., 2016). Spallogenic production rate uncertainty has not been
456 included in the modelling. Muogenic production with depth, including an assumed 8% uncertainty,
457 followed Model 1A from Balco (2017). We assume bulk density to be constant with depth but sampled
458 from a normal distribution of $1.7 \pm 0.1 \text{ g cm}^{-3}$ based on bulk density measured from two core samples
459 for loose sediment, and ice cemented permafrost. ~~In most cases, the ice lenses were less than 5 cm thick.~~
460 ~~The change of density in these thin ice lenses is not included in our assumed bulk density and we~~
461 ~~acknowledge the small difference this assumption could have on the overall model outputs.~~ Erosion rate
462 and net erosion were constrained between 0–0.4 cm/ka and 400 cm, respectively, based on field

463 observations described in Sect. 4.32. Within these constraints, exposure age, surface erosion rate, and
 464 inheritance for ^{10}Be and ^{26}Al were simulated with uniform distributions, and model output was based on
 465 $n=100,000$ acceptable depth profile solutions.

466

467

468 **Table 1.** Depth profile data from Pearse Valley and lower Wright Valley

<u>Sample name</u>	<u>Sample depth (m)</u>	<u>^{10}Be conc. (10^6 atoms g^{-1})^a</u>	<u>^{26}Al conc. (10^6 atoms g^{-1})^b</u>	<u>$^{26}\text{Al}/^{10}\text{Be}$ ratio</u>
<u>Pearse Valley</u>				
<u>PV14-SS-5</u>	<u>0.02 - 0.07</u>	<u>4.24 ± 0.095</u>	<u>-</u>	<u>-</u>
<u>PV14-A-01</u>	<u>0.07 - 0.27</u>	<u>4.37 ± 0.097</u>	<u>18.67 ± 0.73</u>	<u>4.27 ± 0.19</u>
<u>PV14-A-02</u>	<u>0.27 - 0.37</u>	<u>4.35 ± 0.097</u>	<u>17.97 ± 0.71</u>	<u>4.13 ± 0.19</u>
<u>PV14-A-03</u>	<u>0.37 - 0.47</u>	<u>4.42 ± 0.098</u>	<u>19.63 ± 0.82</u>	<u>4.44 ± 0.21</u>
<u>PV14-A-04</u>	<u>0.47 - 0.56</u>	<u>-</u>	<u>19.94 ± 0.78</u>	<u>-</u>
<u>PV14-A-05</u>	<u>0.56 - 0.65</u>	<u>4.40 ± 0.098</u>	<u>18.28 ± 0.69</u>	<u>4.16 ± 0.18</u>
<u>PV14-A-07</u>	<u>0.73 - 0.86</u>	<u>3.96 ± 0.089</u>	<u>17.95 ± 0.70</u>	<u>4.53 ± 0.20</u>
<u>PV14-A-10</u>	<u>1.09 - 1.21</u>	<u>-</u>	<u>16.38 ± 0.64</u>	<u>-</u>
<u>PV14-A-15</u>	<u>1.56 - 1.65</u>	<u>3.80 ± 0.085</u>	<u>15.09 ± 0.59</u>	<u>3.97 ± 0.18</u>
<u>PV14-A-20</u>	<u>2.09 - 2.18</u>	<u>3.98 ± 0.080</u>	<u>17.50 ± 0.66</u>	<u>4.40 ± 0.19</u>
<u>PV14-A-25</u>	<u>2.55 - 2.64</u>	<u>3.85 ± 0.086</u>	<u>16.70 ± 0.66</u>	<u>4.33 ± 0.20</u>
<u>PV14-A-30</u>	<u>3.06 - 3.16</u>	<u>-</u>	<u>16.76 ± 0.66</u>	<u>-</u>
<u>Lower Wright Valley</u>				
<u>WV14-SS-01</u>	<u>0 - 0.02</u>	<u>4.10 ± 0.092</u>	<u>22.89 ± 0.89</u>	<u>5.58 ± 0.25</u>
<u>WV14-I-01</u>	<u>0.07 - 0.23</u>	<u>3.73 ± 0.175</u>	<u>19.04 ± 0.75</u>	<u>5.10 ± 0.31</u>
<u>WV14-I-02</u>	<u>0.23 - 0.35</u>	<u>3.92 ± 0.088</u>	<u>18.43 ± 0.72</u>	<u>4.70 ± 0.21</u>
<u>WV14-I-03</u>	<u>0.35 - 0.43</u>	<u>4.00 ± 0.089</u>	<u>20.38 ± 0.77</u>	<u>5.09 ± 0.22</u>
<u>WV14-I-04</u>	<u>0.43 - 0.54</u>	<u>-</u>	<u>22.72 ± 0.89</u>	<u>-</u>
<u>WV14-I-05</u>	<u>0.54 - 0.63</u>	<u>-</u>	<u>21.66 ± 0.85</u>	<u>-</u>
<u>WV14-I-07</u>	<u>0.69 - 0.78</u>	<u>-</u>	<u>19.99 ± 0.79</u>	<u>-</u>
<u>WV14-I-10</u>	<u>0.98 - 1.07</u>	<u>4.09 ± 0.091</u>	<u>20.54 ± 0.81</u>	<u>5.02 ± 0.23</u>
<u>WV14-I-14</u>	<u>1.56 - 1.62</u>	<u>-</u>	<u>20.62 ± 0.81</u>	<u>-</u>
<u>WV14-I-20</u>	<u>2.02 - 2.14</u>	<u>4.22 ± 0.094</u>	<u>21.80 ± 0.86</u>	<u>5.17 ± 0.23</u>
<u>WV14-I-23</u>	<u>2.36 - 2.45</u>	<u>-</u>	<u>21.41 ± 0.84</u>	<u>-</u>
<u>WV14-I-29</u>	<u>2.80 - 2.91</u>	<u>-</u>	<u>13.60 ± 0.53</u>	<u>-</u>

469

We assume a constant bulk density of $1.7 \pm 0.1 \text{ g cm}^{-3}$ based on bulk density measurements made on two core samples.

Topographic shielding is 0.9932 for Pearse Valley, and 0.9968 for lower Wright Valley, respectively.

^a Normalised to the 07KNSTD (KN-5.2) standard of Nishiizumi et al. (2007).

^b Normalised to the KNSTD (KN-4.2) standard of Nishiizumi (2004).

470

Table 21. Cosmogenic ^{10}Be and ^{26}Al concentrations and apparent exposure ages from Pearse Valley

Sample name	Latitude (DD)	Longitude (DD)	Elevation (masl)	Sample thickness (cm)	Topographic shielding	^{10}Be conc. (10^5 atoms g^{-1}) ^a	^{26}Al conc. (10^5 atoms g^{-1}) ^b	Apparent ^{10}Be exposure age (ka) ^{c,d}	Apparent ^{26}Al exposure age (ka) ^{c,d}	$^{26}\text{Al}/^{10}\text{Be}$ ratio	Erosion-corrected ^{10}Be exposure age (ka) ^e
PV14-CS3-P1	-77.70737	161.55283	451	6	0.993	12.40 ± 0.39	76.57 ± 4.48	158 ± 11 (5)	142 ± 16 (9)	6.18 ± 0.41	174 ± 13 (6)
PV14-CS3-P2	-77.70737	161.55283	451	3	0.993	5.36 ± 0.15	37.99 ± 1.54	65 ± 4 (2)	66 ± 7 (3)	7.09 ± 0.35	68 ± 5 (2)
PV14-CS4-P1	-77.70747	161.55582	451	5	0.993	5.94 ± 0.16	33.71 ± 5.14	74 ± 5 (2)	60 ± 11 (9)	5.68 ± 0.88	77 ± 5 (2)

All samples are granite cobbles and have a density of 2.65 g cm^{-3} .

^a Normalised to the 07KNSTD (KN-5.2) standard of Nishiizumi et al. (2007).

^b Normalised to the KNSTD (KN-4.2) standard of Nishiizumi (2004).

^c Exposure ages calculated using the CRONUS-Earth calculator (<http://hess.ess.washington.edu/math/>), using the LSDn scaling scheme.

^d Both internal and external uncertainties (shown at the 1σ level). Internal uncertainties (given in parentheses) are analytical uncertainties only and external uncertainties are absolute uncertainties and include production rate and scaling errors.

^e Calculated using an erosion rate of 0.65 mm/ka .

Table 2. Depth profile data from Pearse Valley and Lower Wright Valley

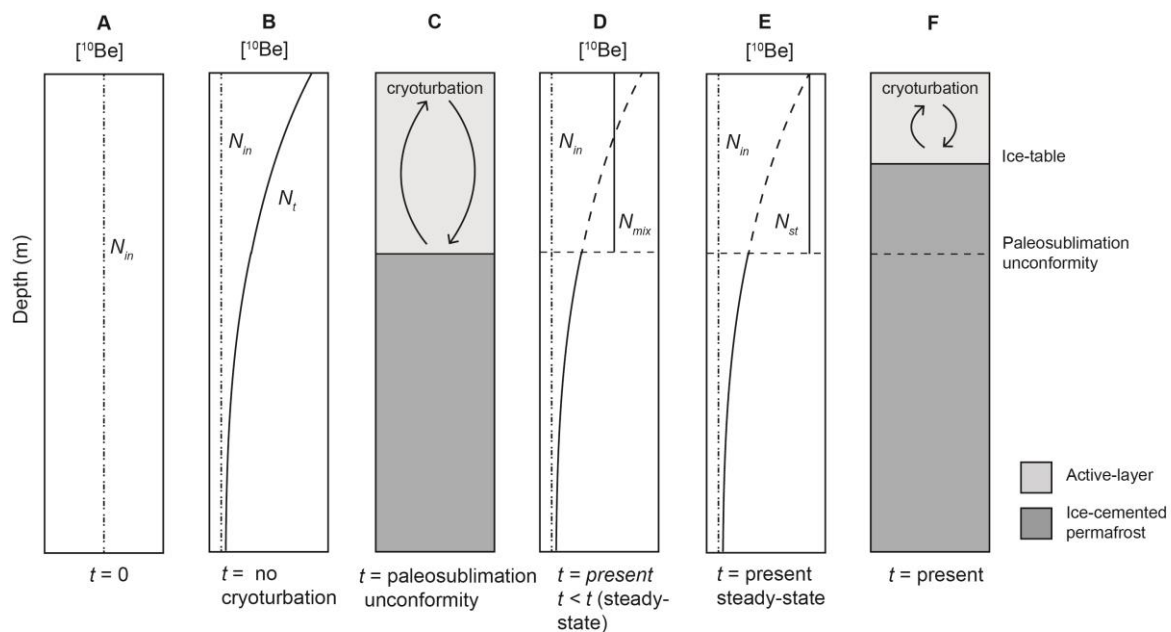
Sample name	Sample depth (m)	^{10}Be conc. (10^6 atoms g^{-1}) ^a	^{26}Al conc. (10^6 atoms g^{-1}) ^b	$^{26}\text{Al}/^{10}\text{Be}$ ratio
Pearse Valley				
PV14 SS-5	0.02–0.07	4.24 ± 0.095	-	-
PV14 A-01	0.07–0.27	4.37 ± 0.097	18.67 ± 0.73	4.27 ± 0.19
PV14 A-02	0.27–0.37	4.35 ± 0.097	17.97 ± 0.71	4.13 ± 0.19
PV14 A-03	0.37–0.47	4.42 ± 0.098	19.63 ± 0.82	4.44 ± 0.21
PV14 A-04	0.47–0.56	-	19.94 ± 0.78	-
PV14 A-05	0.56–0.65	4.40 ± 0.098	18.28 ± 0.69	4.16 ± 0.18
PV14 A-07	0.73–0.86	3.96 ± 0.089	17.95 ± 0.70	4.53 ± 0.20
PV14 A-10	1.09–1.21	-	16.38 ± 0.64	-
PV14 A-15	1.56–1.65	3.80 ± 0.085	15.09 ± 0.59	3.97 ± 0.18
PV14 A-20	2.09–2.18	3.98 ± 0.080	17.50 ± 0.66	4.40 ± 0.19
PV14 A-25	2.55–2.64	3.85 ± 0.086	16.70 ± 0.66	4.33 ± 0.20
PV14 A-30	3.06–3.16	-	16.76 ± 0.66	-
Lower Wright Valley				
WV14 SS-01	0–0.02	4.10 ± 0.092	22.89 ± 0.89	5.58 ± 0.25
WV14 I-01	0.07–0.23	3.73 ± 0.175	19.04 ± 0.75	5.10 ± 0.31
WV14 I-02	0.23–0.35	3.92 ± 0.088	18.43 ± 0.72	4.70 ± 0.21
WV14 I-03	0.35–0.43	4.00 ± 0.089	20.38 ± 0.77	5.09 ± 0.22
WV14 I-04	0.43–0.54	-	22.72 ± 0.89	-
WV14 I-05	0.54–0.63	-	21.66 ± 0.85	-
WV14 I-07	0.69–0.78	-	19.99 ± 0.79	-
WV14 I-10	0.98–1.07	4.09 ± 0.091	20.54 ± 0.81	5.02 ± 0.23
WV14 I-14	1.56–1.62	-	20.62 ± 0.81	-
WV14 I-20	2.02–2.14	4.22 ± 0.094	21.80 ± 0.86	5.17 ± 0.23
WV14 I-23	2.36–2.45	-	21.41 ± 0.84	-
WV14 I-29	2.80–2.91	-	13.60 ± 0.53	-

We assume a constant bulk density of $1.7 \pm 0.1 \text{ g cm}^{-3}$ based on bulk density measurements made on two core samples.

Topographic shielding is 0.9932 for Pearse Valley, and 0.9968 for Lower Wright Valley, respectively.

^aNormalised to the 07KNSTD (KN-5.2) standard of Nishiizumi et al. (2007).

^bNormalised to the KNSTD (KN-4.2) standard of Nishiizumi (2004).



476

477 **Figure 76.** Schematic representation of a ^{10}Be depth profile in permafrost modified by active-layer
 478 cryoturbation. (a) Initial ^{10}Be profile (constant with depth) in well-mixed glacial till or sediment. All
 479 quartz grains are assumed to have been deposited with a common nuclide inheritance (N_{in}). (b) After
 480 prolonged exposure and in the absence of sediment mixing, an exponentially decreasing nuclide depth
 481 profile is obtained. (c) Permafrost profile during an interval where air temperature is warmer than
 482 present allowing near surface sediments to form an active-layer above the paleo-sublimation depth.
 483 Sediments below the unconformity are perennially frozen. (d & e) Vertical mixing via active-layer
 484 cryoturbation results in an average ^{10}Be value (N_{mix}) (d), and (N_{st}) with steady-state erosion (e). An
 485 exponentially decreasing ^{10}Be profile remains below the unconformity. (f) Present-day permafrost
 486 profile with shallower active-layer and ice-table than shown in (c).

487

488 4 Results

489 4.1 Surface exposure ages and erosion rates at Pearse Valley

490 ~~Boulders and cobbles of granite, gneiss, Beacon sandstone and dolerite pepper the Pearse Valley floor,~~
 491 ~~forming a thin, patchy drift overlying an older, well weathered relict drift surface. Some boulders~~
 492 ~~lodged in the relict drift host smaller perched boulders, cobbles, and pebbles on their surfaces, indicating~~
 493 ~~deposition of perched clasts occurred after the most recent retreat of Taylor Glacier (Fig. 4).~~

494

495 ~~Our surface exposure chronology is based on three granitic cobbles on the northern side of the central~~
 496 ~~valley floor (Table 1, Fig. 2). Two samples (PV14 CS3 P2 and PV14 CS4 P1) yielded minimum zero~~
 497 ~~erosion ^{10}Be exposure ages of 65 ± 4 ka and 74 ± 5 ka (1 σ external errors), respectively, whereas the~~
 498 ~~third sample (PV14 CS3 P1) yielded an older age of 158 ± 11 ka, presumably affected by inheritance~~
 499 ~~(Table 1). The three $^{26}\text{Al}/^{10}\text{Be}$ concentration ratios range from 5.7 to 7.1 and when plotted on ^{10}Be -~~
 500 ~~$^{26}\text{Al}/^{10}\text{Be}$ diagram, largely indicates a simple exposure within their 1 σ error ellipses without any prior~~

501 complex history (Fig. 7). While this assumption of zero erosion makes negligible difference for LGM
502 and younger ages, we evaluate the influence of surface erosion on the exposure ages above using known
503 erosion rates reported from Antarctica and geological evidence from the sites. Bedrock and regolith
504 erosion rates in the Dry Valleys range from 0.1–4 mm/ka (Putkonen et al., 2008; Summerfield et al.,
505 1999). A compiled study across Antarctica showed that granite populations have a mean erosion rate of
506 0.13 mm/ka, and in the Dry valleys, a max erosion rate of 0.65 mm/ka (Marrero et al., 2018). Applying
507 the max erosion rate (0.65 mm/ka) from granite surfaces in the Dry Valleys, erosion corrected ^{10}Be
508 exposure ages of our granitic cobbles resulted in 174 ± 13 ka (PV14 CS3 P1), 68 ± 5 ka (PV14 CS3-
509 P2) and 77 ± 5 ka (PV14 CS4 P1) (1σ external errors; Table 1). The cobble sample PV14 CS3 P2
510 displays minimal edge rounding which suggests negligible erosion and is unlikely to be much older
511 than the zero erosion age.

512 **Figure 7.** Two isotope plot of Pearse Valley cobbles. Nuclide concentrations with 1σ uncertainties,
513 using the time-dependent LSDn scaling scheme of Lifton et al. (2014). Burial isochrons (dotted lines),
514 decay trajectories (dashed), the exposure erosion region (bounded by black and red lines), and steady-
515 state erosion loci (green) are shown.

517 **4.2 Cosmogenic nuclide depth profiles at Pearse Valley**

518 **4.1 Cosmogenic nuclide depth profiles**

519 Both the Pearse Valley (Fig. 4), and lower Wright Valley (Fig. 5) depth profiles share two common
520 observations. Neither depth profile displays a marked exponential decrease in measured nuclide
521 concentration over the full ~3 m core depth profile, and both cores have shallow, active mixed-layers
522 where measured nuclide concentrations are effectively constant.

523 In the Pearse Valley permafrost core, there is a marked decrease in all ^{10}Be and ^{26}Al concentrations for
524 samples below ~0.65 m depth. However, the reduction in ^{10}Be (and ^{26}Al) between shallow (active-layer)
525 and deep samples from only ~ 4.4 to $\sim 3.8 \times 10^6$ atoms g^{-1} (and respectively from ~ 19.9 to $\sim 15.1 \times 10^6$
526 atoms g^{-1} for ^{26}Al) indicates a high inherited cosmogenic concentration supporting a marginal post-
527 depositional increase of ^{10}Be and ^{26}Al . Moreover, the average $^{26}\text{Al}/^{10}\text{Be}$ ratio which ranges between 4.0
528 to 4.5 suggests a long history of total exposure and burial for these permafrost sediments (i.e., in addition
529 to their presence in the core as permafrost). One feature worthy of note, is the distinct increase in both
530 ^{10}Be and ^{26}Al for the deepest three samples below 2.09 m depth compared to samples <1.65 m depth,
531 suggesting that the Pearse Valley permafrost core may not have been a single depositional event. In
532 contrast, the lower Wright Valley depth profiles for ^{10}Be and ^{26}Al show more scatter than the Pearse
533 Valley depth profiles and there is no decrease in concentration with depth. Effectively the lower Wright
534 Valley profile is depth independent with a ^{10}Be concentration at $\sim 4.0 \times 10^6$ and a ^{26}Al concentration at
535 $\sim 20.3 \times 10^6$ atoms g^{-1} . The magnitudes of the concentrations for Pearse and Wright valleys are

536 remarkably similar, as is the range in $^{26}\text{Al}/^{10}\text{Be}$ ratio from 4.7 to 5.6, suggesting that lower Wright
537 Valley permafrost sediments have had a similar total exposure-burial history as Pearse Valley
538 sediments.

539 These depth profiles present complications to any modelling aiming for non-unique solutions of
540 deposition age and surface erosion due to the presence of a surface mixed-layer and marginal (in Pearse
541 Valley) to near absent (in lower Wright Valley) post-depositional build-up of ^{10}Be and ^{26}Al in the shallow
542 subsurface sediments. We note that applying a depth profile model that assumes nuclide concentration
543 attenuation to a profile that contains a surface mixed-layer and depth concentration inversions has
544 limitations with respect to chronological information. In the following sections we describe the modified
545 depth modelling exercises taken to accommodate the complication presented in the Pearse Valley and
546 lower Wright Valley data sets.

548 **4.2 Minimum age estimate for Pearse Valley core**

549 Prior to any depth profile modelling, a simple calculation was carried out to estimate the depositional
550 age of the upper ~0.65 m of the Pearse Valley permafrost by comparing maximum and minimum
551 nuclide concentrations. Assuming zero erosion and a surface production rate determined at the coring
552 site, a minimum ‘exposure age’ (t_{min}) can be calculated using the following equation:

$$553 \quad t_{min} = (N_{max} - N_{min}) / P \quad (1)$$

554 Where N_{max} is the absolute maximum ^{10}Be concentration, N_{min} is the absolute minimum ^{10}Be
555 concentration (assumed inheritance) for all mixed sediments, and P is the production rate (atoms g^{-1}) at
556 the sample site. The absolute maximum and minimum ^{10}Be concentrations for the Pearse Valley depth
557 profile using equation 1 are reported in Table 3. Equation 1 yielded a minimum deposition age of ~74
558 ka for the Pearse Valley core (Table 3).

559 **Table 3.** Maximum and minimum ^{10}Be concentrations and minimum deposition age for the Pearse Valley core.

Borehole	P	N_{max} (10^6 atoms g^{-1})	N_{min} (10^6 atoms g^{-1})	Min age (ka)
PV14-A	8.4	4.42	3.80	74

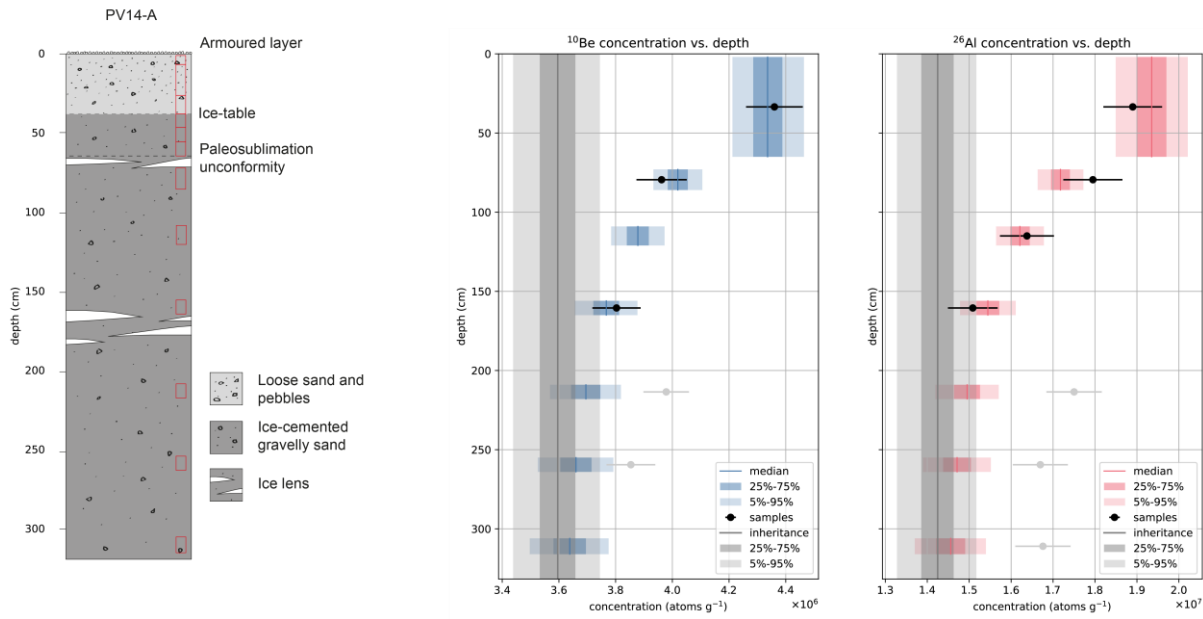
561 **4.3 Cosmogenic nuclide depth profiles at Pearse Valley**

562 The ^{10}Be and ^{26}Al depth profiles from the permafrost core and overlying active layer at Pearse Valley,
563 and associated modelled nuclide concentrations from a best fit to all samples are shown in Fig. 8. No
564 acceptable depth profile model fit was obtained for all measured ^{10}Be and ^{26}Al depth profile samples
565 (see Fig. 8). However, the model appears to have performed better for the deeper samples ≥ 2.09 m, than
566 for the shallower samples < 1.65 m. Below the surface mixed-layer, between 0.65 m and 1.65 m, both

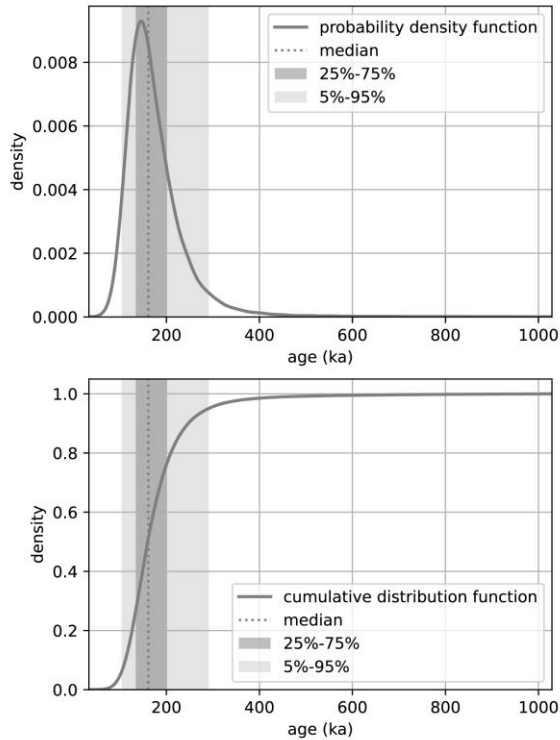
567 ¹⁰Be and ²⁶Al concentrations display attenuation with depth. Below 1.65 m, the attenuation is interrupted
568 by a considerable increase in nuclide concentrations from 2.09 m depth. This ~~result~~ suggests that the
569 depth profile is of a composite structure, ~~which. This~~ is supported by the observation that ice lenses
570 appearing at ~0.7 m, and at ~1.70–1.80 m (see Fig. 4), ~~which~~ are ~~also~~ associated with distinct changes
571 in ¹⁰Be and ²⁶Al concentrations. No acceptable depth profile model fit was obtained when all measured
572 ¹⁰Be and ²⁶Al concentrations were included as a single depositional episode (see Fig. S1). Hence,
573 consideration was given to restrict our depth profile model to only fit samples from 0.02 to 1.65 m
574 depth, and how to incorporate the surface mixed-layer with the depth profile. ~~Between 0.65 m and 1.65~~
575 ~~m, both ¹⁰Be and ²⁶Al cosmogenic nuclide concentrations display attenuation with depth, whilst below~~
576 ~~1.65 m, the attenuation is interrupted by a considerable increase in nuclide concentrations as shown in~~
577 ~~the sample at 2.09 m depth.~~

578 ~~We attempt a model best fit only to the samples above 1.65 m in order to determine the younger~~
579 ~~depositional phase.~~ The five ¹⁰Be and five ²⁶Al nuclide concentrations from 0.02–0.65 m exhibit a
580 uniform concentration with depth with averages of $4.36 \pm 0.10 \times 10^6$ atoms g⁻¹ and $1.89 \pm 0.07 \times 10^7$
581 atoms g⁻¹, respectively, with no attenuation, indicating that these upper sediments have been vertically
582 mixed (or possibly deposited sufficiently recently so that nuclide depth profiles effectively reflect only
583 inheritance without significant post-depositional production). In continuously vertically mixed surface
584 soils (such as those in the McMurdo Dry Valleys), where mixing times are short compared to
585 radionuclide decay rates, the average production rate in the mixed-layer is constant with depth (Granger
586 and Riebe, 2014). Under these conditions, the average cosmogenic nuclide concentration in the mixed-
587 layer will attain a constant value at erosional equilibrium (Fig. 7). To accommodate the vertically-
588 mixed, uniform ¹⁰Be and ²⁶Al concentrations in the upper 0.65 m. Hence, we use the mean ¹⁰Be and ²⁶Al
589 concentrations in the upper 0.65 m from these samples to approximate best represent the surface mixing
590 processes that resulted in the uniform profile. (i.e., a vertically mixed cryoturbated layer or the most
591 recent deposition) as shown in Fig. 89. Fig. 8 shows the model best-fit to samples from 0.02–1.65 m,
592 with all samples between 0.02 and 0.65 m depth converging to a single mean concentration in order to
593 determine the younger depositional phase. When solving for the four free parameters, namely, age,
594 erosion rate, ¹⁰Be and ²⁶Al inheritance, ~~t~~The best-fit modelled nuclide concentrations for the PV14-A
595 depth profile when restricted to samples from 0.02 to 1.65 m depth, falls within the 25th to 75th percentile
596 of the measured concentrations. The reduced chi-squared statistical test for the best-fit to a profile using
597 a mean concentration for the surface mixed-layer with the upper sediment samples (0.02 to 1.65 m
598 depth) gives a value of 0.88 with three degrees of freedom (n=7) which is significantly better than the
599 reduced chi-squared value of 2.70 with 16 degrees of freedom (n=20) for the full profile using all
600 nuclide measurements (0.02 – 3.16 m) (see SD3), confirming our modified approach improved model
601 fitting. We constrained the erosion rate of the depth profiles using information from surface cobble
602 PV14-CS3-P2 which sits ~10–20 cm above the desert pavement and has a minimum exposure age of

603 65 ka (Fig. 6a4a). Based on this observation we can assume a maximum surface lowering rate of ~ 0.3
 604 cm ka^{-1} . Using this field observation, we applied a conservatively high erosion rate limit of 0.4 cm ka^{-1}
 605 for our depth profile modelling. The solutions yield most probable ^{10}Be and ^{26}Al inheritance
 606 concentrations of 3.59×10^6 and 1.42×10^7 atoms g^{-1} , respectively (Fig. 89; Fig S24) and constrain the
 607 depositional age of the sediment permafrost ($<1.65 \text{ m depth}$) at $180^{+20} / -40 \text{ ka}$ (Fig. 949), and an erosion
 608 rate of $0.24^{+0.10} / -0.09 \text{ cm ka}^{-1}$ (Fig. S2). By inference, the lower part of the profile ($>2.09 \text{ m depth}$)
 609 predates the sediments above and must be deposited before $\sim 180 \text{ ka}$.



610
 611 **Figure 8.** Pearse Valley (PV14-A) permafrost core sedimentology (left). Locations of cosmogenic
 612 nuclide samples shown in red boxes. Pearse Valley (PV14-A) permafrost core depth profiles with
 613 measured ^{10}Be and ^{26}Al concentrations (black data points) with 1σ uncertainties (right). For all samples
 614 between $0.02\text{--}0.65 \text{ m depth}$, we used the average concentration of all five ^{10}Be and ^{26}Al measurements
 615 to represent the effect of cryoturbation of sediments in the active-layer. Blue (^{10}Be) and red (^{26}Al) boxes
 616 show simulated nuclide concentrations at each depth. ^{10}Be and ^{26}Al concentrations (grey data points)
 617 below 2.09 m were not included in the model.



618

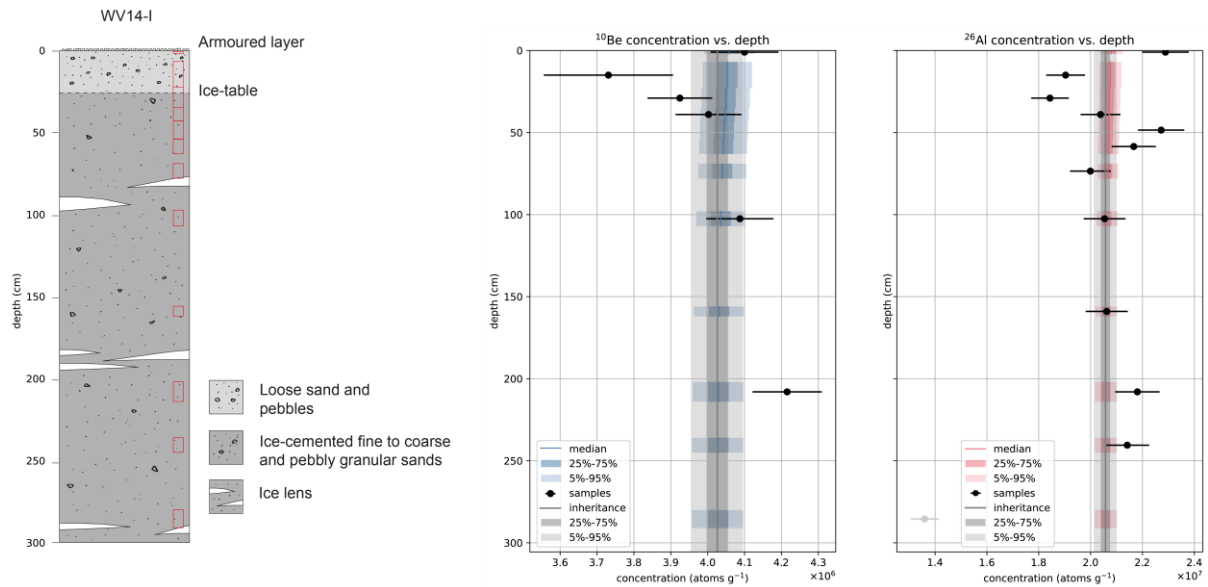
619 **Figure 9.** Probability density function, and cumulative distribution function for exposure age, using
 620 dual-nuclide depth profile modelling between 0.02 – 1.65 m depth for PV14-A.

621

622 **4.43 Cosmogenic nuclide depth profiles at Lower Wright Valley**

623 The ^{10}Be and ^{26}Al depth profiles from the permafrost core and overlying active-layer used for depth
 624 profile modelling at Lower Wright Valley is shown in Fig 104. The Lower Wright Valley ^{10}Be and
 625 ^{26}Al concentration profiles exhibit near-constant concentrations with depth, with average values of 4.01
 626 $\pm 0.10 \times 10^6$ atoms g^{-1} and $2.08 \pm 0.08 \times 10^7$ atoms g^{-1} , respectively. The absence of a discernible
 627 exponential attenuation indicates all sediments in the depth profile are either continuously vertically
 628 mixed after deposition, or are sufficiently young so that post-depositional nuclide production is
 629 negligible relative to inheritance.

630 The depth profile model does not work well for non-attenuating profiles and usually fails to give well-
 631 constrained results. The modelled nuclide concentration depth profiles do not fit within the 5th to 95th
 632 percentile for our measured concentrations in the Lower Wright Valley depth profile (Fig. 104). The
 633 solutions yield most probable ^{10}Be and ^{26}Al inheritance concentrations of 4.03×10^6 and 2.06×10^7 atoms
 634 g^{-1} , respectively (Fig. 104; Fig. S43). Our simulations yield the depositional age of the permafrost at 4.4
 635 $^{+8.2}_{-4.2}$ ka (5th to 95th percentile), and an erosion rate of $0.2^{+0.18}_{-0.18}$ cm ka^{-1} (Fig. S43).



636

637 **Figure 10.** Lower Wright Valley (WV14-I) permafrost core sedimentology (left). Locations of
 638 cosmogenic nuclide samples shown in red boxes. Lower Wright Valley (WV14-I) permafrost core depth
 639 profiles with measured ^{10}Be and ^{26}Al concentrations (black data points) with 1σ uncertainties (right).
 640 Blue (^{10}Be) and red (^{26}Al) boxes show simulated nuclide concentrations at each depth.

641 ~~Figure 9. Pearse Valley (PV14 A) permafrost core depth profiles with measured ^{10}Be and ^{26}Al~~
 642 ~~concentrations (black data points) with 1σ uncertainties. For all samples between 0.02–0.65 m depth,~~
 643 ~~we used the average concentration of all five ^{10}Be and ^{26}Al measurements to represent the effect of~~
 644 ~~eryoturbation of sediments in the active layer. Blue (^{10}Be) and red (^{26}Al) boxes show simulated nuclide~~
 645 ~~concentrations at each depth. ^{10}Be and ^{26}Al concentrations (grey data points) below 2.09 m were not~~
 646 ~~included in the model.~~

647

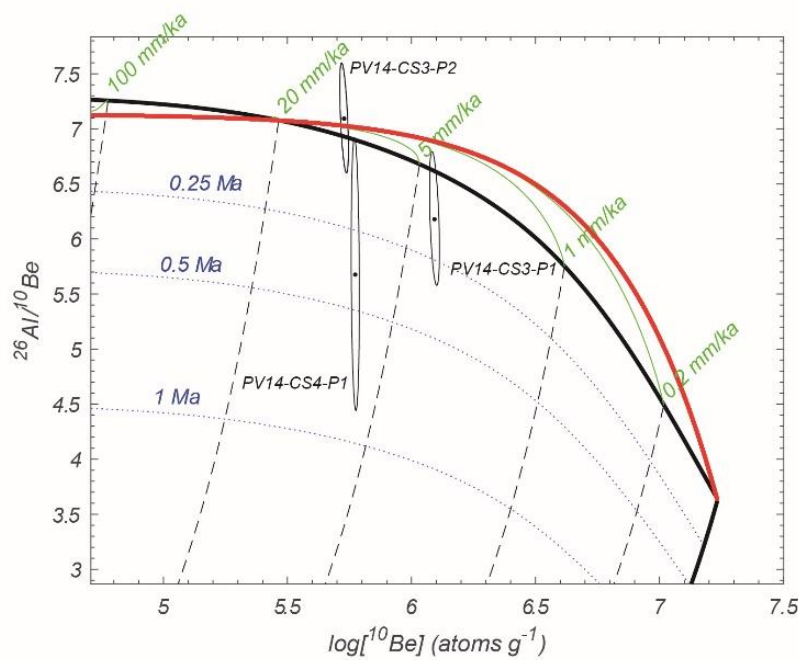
648 ~~Figure 11. Lower Wright Valley (WV14 I) permafrost core depth profiles with measured ^{10}Be and ^{26}Al~~
 649 ~~concentrations (black data points) with 1σ uncertainties. Blue (^{10}Be) and red (^{26}Al) boxes show~~
 650 ~~simulated nuclide concentrations at each depth.~~

651

652 **4.5 Surface exposure ages and erosion rates at Pearse Valley**

653 Boulders and cobbles of granite, gneiss, Beacon sandstone and dolerite pepper the Pearse Valley floor,
 654 forming a thin, patchy drift overlying an older, well-weathered relict drift surface. Some boulders
 655 lodged in the relict drift host smaller perched boulders, cobbles, and pebbles on their surfaces, indicating
 656 deposition of perched clasts occurred after the most recent retreat of Taylor Glacier (Fig. 65). Our
 657 surface exposure chronology is based on three granitic cobbles on the northern side of the central valley
 658 floor (Table 24, Fig. 2). Two samples (PV14-CS3-P2 and PV14-CS4-P1) yielded minimum zero-
 659 erosion ^{10}Be exposure ages of 65 ± 4 ka and 74 ± 5 ka (1σ external errors), respectively, whereas the
 660 third sample (PV14-CS3-P1) yielded an older age of 158 ± 11 ka, presumably affected by inheritance
 661 (Table 24). The three $^{26}\text{Al}/^{10}\text{Be}$ concentration ratios range from 5.7 to 7.1 and when plotted on ^{10}Be -
 662 $^{26}\text{Al}/^{10}\text{Be}$ diagram, are consistent with a simple constant exposure within their 1σ error ellipses (Fig.

663 117). One sample (PV14-CS4-P1) suggests a burial age ranging from 0 up to ~900 ka burial, the result
 664 of a large error in measured ^{26}Al concentration. Given inheritance is stochastic, we infer the two lowest
 665 consistent ages represent the minimum inheritance, and we take them to be our best estimate to represent
 666 zero-erosion exposure ages for the cobbles. While this assumption of zero erosion makes negligible
 667 difference for LGM and younger ages, we evaluate the influence of surface erosion on the exposure
 668 ages above using known erosion rates reported from Antarctica and geological evidence from the sites.
 669 Bedrock and regolith erosion rates in the McMurdo Dry Valleys range from 0.1–4 mm/ka (Putkonen
 670 et al., 2008; Summerfield et al., 1999). A compiled study across Antarctica showed that granite
 671 populations have a mean erosion rate of 0.13 mm/ka, and in the Dry valleys, a max erosion rate of 0.65
 672 mm/ka (Marrero et al., 2018). Applying the max erosion rate (0.65 mm/ka) from granite surfaces in the
 673 McMurdo Dry Valleys, erosion corrected ^{10}Be exposure ages of our granitic cobbles resulted in $174 \pm$
 674 13 ka (PV14-CS3-P1), 68 ± 5 ka (PV14-CS3-P2) and 77 ± 5 ka (PV14-CS4-P1) (1σ external errors;
 675 Table 2). The cobble sample PV14-CS3-P2 displays minimal edge rounding which suggests negligible
 676 erosion and is unlikely to be much older than the zero-erosion age.



677

678 **Figure 110.** Two-isotope plot of Pearse Valley cobbles using the time-dependent LSDn scaling scheme
 679 of Lifton et al. (2014) and the primary default calibration data set of Borchers et al. (2016). Measured
 680 ^{26}Al and ^{10}Be concentrations are shown with 1σ uncertainties, using the time-dependent LSDn scaling
 681 scheme of Lifton et al. (2014). Burial isochrons (dotted lines), decay trajectories (dashed), the exposure-
 682 erosion region (bounded by black and red lines), and steady-state erosion loci (green) are shown.

683

684 5 Discussion

685 5.1 Depositional and permafrost processes at Pearse Valley

686 ~~Thin, patchy drift at Pearse Valley is a discontinuous peppering of boulders and cobbles superimposed~~
687 ~~on older loose sandy sediments, reworked clasts, and underlying permafrost sediments (Fig. 4). Surface~~
688 ~~cobble exposure ages confirm that this thin, patchy drift was deposited by a retreating cold-based Taylor~~
689 ~~Glacier during MIS 5a, and the MIS 5 / 4 transition, and corresponds with Taylor 2 Drift in central~~
690 ~~Taylor Valley.~~ Depth profile modelling ~~suggests~~confirms that the permafrost sediments underlying
691 Taylor 2 Drift, at Pearse Valley, predate MIS 5. ~~Undisturbed preservation of these relict surfaces is~~
692 ~~consistent with cold-based glacier activity described by Atkins (2013).~~

693 At the PV14-A permafrost core site, the present-day active-layer comprises a desert pavement surface
694 and layer of loose vertically mixed sediments to a depth of ~0.37 m, positioned above ice-cemented
695 permafrost sediments. The interface between this active-layer and the ice-cemented permafrost
696 represents a sublimation unconformity. ^{10}Be and ^{26}Al concentrations are constant throughout the active
697 layer and down to ~0.65 m depth in the permafrost. However, there is a discernible decrease in ^{10}Be and
698 ^{26}Al concentrations in the permafrost ~~below~~at ~0.65 m depth alongside an ice horizon (Fig. 4). Such ice
699 horizons are indicative of a paleosublimation unconformity, and ~~the presence of a paleosublimation~~
700 ~~unconformity~~ suggests the sediments experienced intervals that are warmer than present-day during or
701 after deposition. This ^{10}Be ~~reduction~~offset cannot be explained by active-layer cryoturbation, as the
702 present-day active-layer is only 0.37 m deep. Lapalme et al. (2017) suggested that in the upper ~0.5 m
703 of a soil profile, ice can accumulate and sublimate due to changing ground surface temperature and
704 humidity conditions. Below ~0.5 m depth, ice will progressively increase over time. Therefore, a
705 paleosublimation unconformity can be inferred by the increase in ice content from 0.69 to 0.40 ~~em~~ depth,
706 which records the maximum predicted ice table depth (Lapalme et al., 2017). Therefore, we suggest the
707 ^{10}Be ~~reduction~~offset between the sediments above and below 0.65 m represent a paleosublimation
708 unconformity ~~(Fig. 5a, 8)~~ which probably ~~formed~~occurred when the active-layer was thicker than
709 present. However, we cannot rule out that the fluctuation of the present-day active-layer depth through
710 summer months could represent annual variability of the active-layer. Although, the lack of active-layer
711 thickness exceeding >50 cm depth in low elevation McMurdo Dry Valleys locations (Bockheim et al.,
712 2007) suggests this is unlikely in Pearse Valley which is further inland and at higher elevation.
713 Gravimetric water content is relatively high in near-surface permafrost in the McMurdo Dry Valleys
714 (Lacelle et al., 2022), and water content in permafrost influences the susceptibility of cryoturbation. Our
715 depth profile model indicates that the upper section of the Pease Valley permafrost sediments (<1.65 m)
716 was likely deposited at $180^{+20} / -40$ ka, which does not contradict the exposure ages of the thin, patchy
717 drift (~65–74 ka). Our measured nuclide concentrations at >2.09 m depth largely differ from the upper
718 section and do not fit the simulated depth profile constrained between 0.02 and 1.65 m depth (Fig. 89).
719 The ~~increase in~~higher nuclide concentrations at >2.09 m depth relative to the samples between 1.09–1.65
720 m depth in these samples, alongside the presence of several small ice lenses between 1.57–1.87 m depth,
721 suggest these sediments were deposited during an earlier depositional event before ~180 ka. If the lower

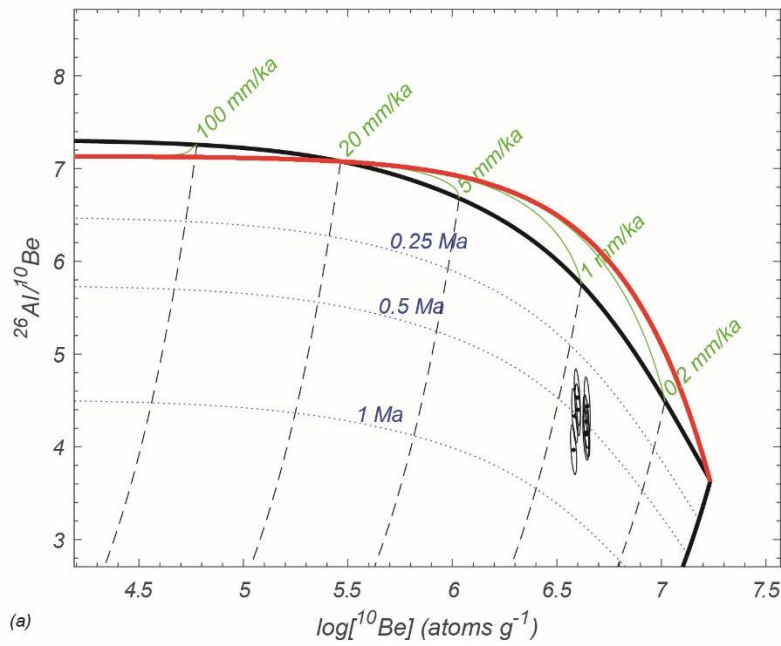
722 set of ice lenses (1.57–1.87 m depth) represent the bottom of a paleoactive-layer, this would imply ~0.5–
723 0.8 m of erosion prior to the most recent episode of sediment deposition above 1.65 m. The
724 sedimentology of the core lacks evidence to suggest if this scenario is plausible or not. The attenuating
725 depth profile (>0.65 m depth) shows that sediments at Pearse Valley have not been vertically mixed since
726 MIS 5, but the surface mixing has occurred to at least 0.65 m depth in the last ~749–102 ka.

727 There are several complications/limitations regarding modelling the permafrost-of the depth profiles that
728 limit the reliability in calculating deposition age and surface erosion rates. data worth noting Firstly,
729 Pearse Valley is episodically covered by ice from Taylor Glacier advances. During these intervals
730 periods of ice cover, vertical mixing does not occur. Secondly, using a mean concentration for the
731 measured samples in the surface mixed-layer (0.02–0.65 m depth) is equivalent to assuming the mean
732 value can represent a constant well-mixed layer-equivalent to a non-mixed deposit. We acknowledge
733 using a mixing model (e.g. Knudsen et al., 2019; Lal & Chen, 2005) for the depth profile data would
734 allow an alternate approach, and may provide an improved fit, among many possible scenarios. However,
735 given the complexity of these data and uncertainty of ice cover by Taylor Glacier, which cannot be
736 incorporated in other mixing models, simply using the mean concentration within the upper 0.65 m is a
737 reasonable approximation.

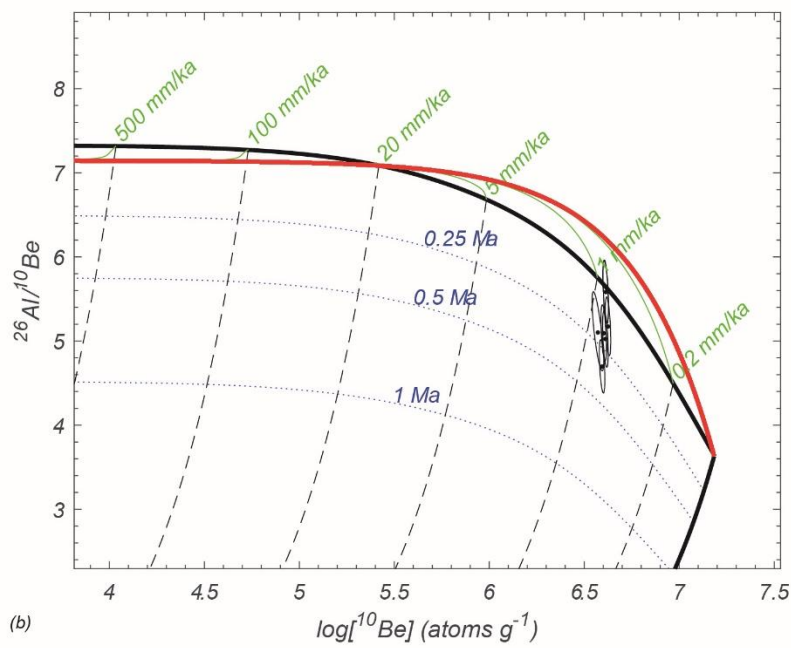
738
739 **Figure 12.** Two isotope plot of Pearse Valley (a) and Lower Wright Valley (b) depth profiles Nuclide
740 concentrations with 1 σ uncertainties, using the time dependent LSDn sealing scheme of Lifton et al.
741 (2014). Burial isochrons (dotted lines), decay trajectories (dashed), the exposure-erosion region
742 (bounded by black and red lines), and steady state erosion loci (green) are shown.

744 5.2 Exposure-burial history of sediments in Pearse Valley and Lower Wright Valley

745 While nuclide depth profiles indicate the most recent depositional history of the permafrost sediment,
746 $^{26}\text{Al}/^{10}\text{Be}$ ratio data provides an additional insight regarding the total history of the sediment. When
747 $^{26}\text{Al}/^{10}\text{Be}$ is plotted against ^{10}Be concentration on a two-isotope diagram (Fig. 12), a minimum total
748 exposure-burial period can be inferred on the assumption that the sample experienced only one cycle of
749 continuous exposure followed by continuous deep burial. At the Pearse Valley site, the two-isotope plot
750 indicates that all sediments, regardless of their depth, have $^{26}\text{Al}/^{10}\text{Be}$ ratios ranging from 3.97 to 4.53,
751 resulting in a minimum ~800 ka simple exposure (at zero erosion), and minimum ~400 ka burial, with
752 a total exposure-burial history of at least 1.2 Ma. At the Lower Wright Valley site, $^{26}\text{Al}/^{10}\text{Be}$ ratios for
753 all samples range from 4.70 to 5.58, resulting in a minimum ~900 ka simple exposure, and minimum
754 ~300 ka burial, with a total exposure-burial history of at least 1.2 Ma. These exposure-burial histories
755 from the two-isotope plots for the Pearse and lower Wright valleys depth profiles assume that the
756 surface production rate at each of the core elevations represents a minimum value.



(a)



(b)

757

758 **Figure 12.** Two-isotope plot of Pearse Valley (a) and lower Wright Valley (b) depth profiles using the
 759 time-dependent LSDn scaling scheme of Lifton et al. (2014) and the primary default calibration data
 760 set of Borchers et al. (2016). Measured nuclide concentrations are shown with 1σ uncertainties. Burial
 761 isochrons (dotted lines), decay trajectories (dashed), the exposure-erosion region (bounded by black
 762 and red lines), and steady-state erosion loci (green) are shown. The exposure-erosion regions are
 763 produced using the surface production rates of 8.40 atoms g⁻¹ yr⁻¹ for Pearse Valley, and 7.47 atoms g⁻¹
 764 yr⁻¹ for lower Wright Valley, respectively.

765 Depth profile modelling ages of near-surface sediments at both permafrost core sites represent the most
 766 recent phase of their depositional histories. ~~For~~ Pearse Valley permafrost sediments were emplaced this

767 ~~occurred at ~180 ka, using a best-fit surface erosion rate of 0.24 cm ka⁻¹.~~ ~~and for Lower Wright Valley,~~
768 where ¹⁰Be and ²⁶Al concentrations do not attenuate, depth profile modelling is not useful in determining
769 age. Instead, we estimate a maximum deposition age of <25 ka. This age represents the time required to
770 change ¹⁰Be and ²⁶Al above the initial inheritance level for near-surface samples by 5% - a change outside
771 AMS ¹⁰Be and ²⁶Al measurement error. However, our ²⁶Al/¹⁰Be ratios at both sites suggest that these
772 sediments have much longer total exposure-burial histories of at least 1.2 Ma, which most likely involves
773 multiple recycling episodes of exposure, deposition, burial, and deflation prior to deposition at their
774 current locations. Million-year exposure-burial recycling periods of sediments in the McMurdo Dry
775 Valleys was also observed in shallow (<1 m) pits from the Packard Dune fields in Victoria Valley (Fink
776 et al., 2015).

777 In summary, Pearse Valley sediments are old, have a complex exposure-burial history >1.2 Ma, were
778 recently deposited ~180 ka, and their shallow-surface sediments (<0.65 m depth) were subject to active-
779 layer mixing. Lower Wright Valley sediments are equally old, with a similar exposure-burial history, but
780 were deposited and mixed after the LGM.

781

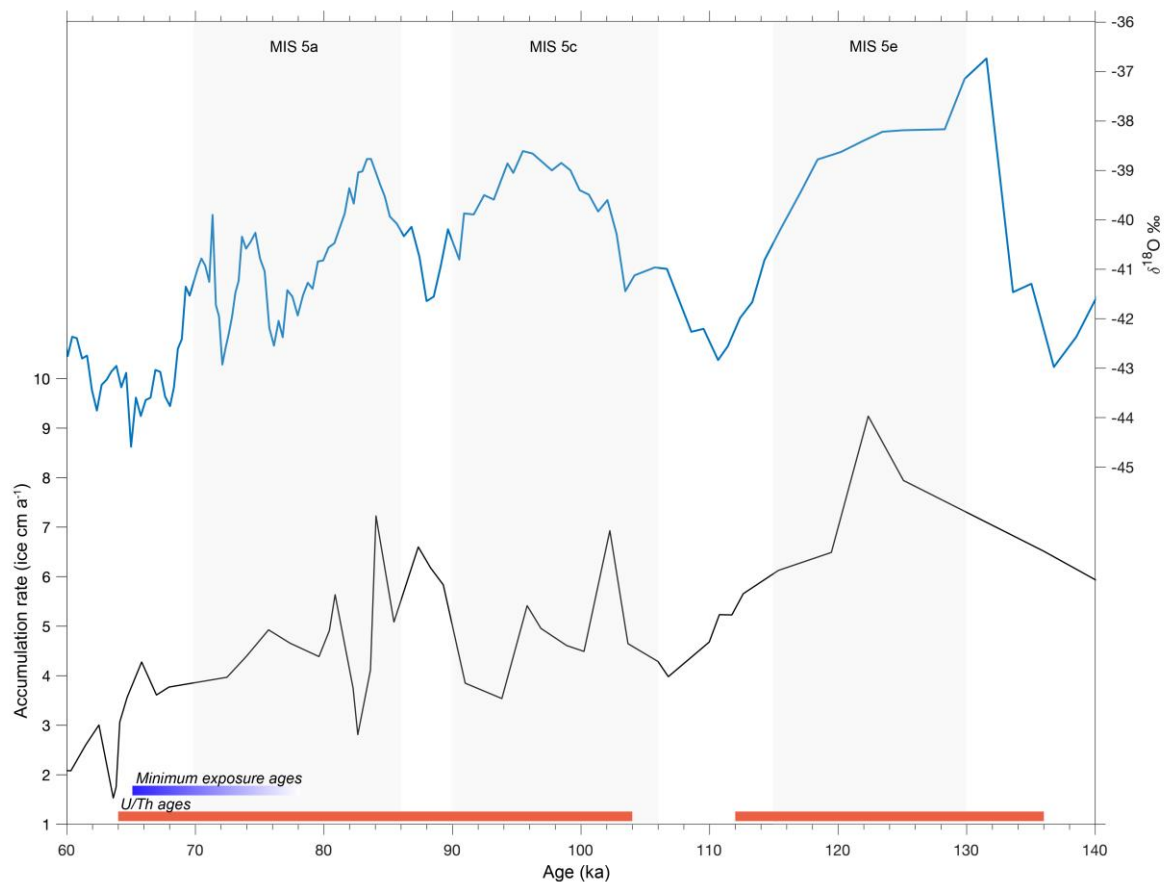
782 **5.3 Fluctuations of Taylor Glacier in Pearse Valley during MIS 5**

783 Thin, patchy drift at Pearse Valley is a discontinuous peppering of boulders and cobbles superimposed
784 on older loose sandy sediments, reworked clasts, and underlying permafrost sediments (Fig. 6).
785 Exposure ages of surface cobbles perched on large boulders confirm that this thin, patchy drift was
786 deposited by a retreating cold-based Taylor Glacier during MIS 5a, and the MIS 5 / 4 transition, on the
787 northern valley floor of central Pearse Valley, whereas the underlying permafrost sediments were
788 deposited at ~180 ka or earlier.

789 ~~Surface exposure ages of the cobbles perched on large boulders together with constraints from a best-~~
790 ~~fit depth profile age indicate Taylor 2 Drift sediments were deposited ~65–74 ka, during MIS 5a, and~~
791 ~~the MIS 5 / 4 transition, on the northern valley floor of central Pearse Valley, whereas the underlying~~
792 ~~permafrost sediments were deposited at ~180 ka or earlier.~~ Our surface cobble geochronology is in
793 agreement with the minimum U/Th ages for the extent of proglacial Lake Bonney, which suggest retreat
794 of Taylor Glacier following MIS 5c and 5a advance (Fig. 13; Higgins et al., 2000a), and the tentatively
795 dated western section of the rock glacier derived from $\delta^{18}\text{O}$ in buried ice in northern Pearse Valley
796 (Swanger et al., 2019). These data suggest Pearse Valley was largely or partially glaciated throughout
797 MIS 5c and 5a.

798 Retreat of the Taylor Glacier lobe in Pearse Valley possibly continued after 65 ka. Timing of retreat
799 after 65 ka, until the Last Glacial Maximum, where Taylor Glacier was at a minimum position, remains
800 unknown. Advance and retreat cycles during MIS 5, the final retreat of Taylor Glacier during MIS 5a,

801 and between the MIS 5 / 4 transition and the LGM for Taylor Glacier, could be better constrained by
 802 exposure dating more drift deposits with larger spatial coverage from Pearse Valley.



803
 804 **Figure 13.** Snow accumulation rate (ice cm a^{-1}) determined from ^{10}Be ($\text{Acc. (ice cm a}^{-1}\text{)}$) and $\delta^{18}\text{O}$
 805 record from Taylor Dome during MIS 5 (Steig et al., 2000). U/Th ages from algal carbonates (red bands,
 806 Higgins et al., 2000a) coincide with warm MIS substages 5e, 5c and 5a with increased accumulation
 807 rates at Taylor Dome. This is consistent with our minimum exposure ages (blue band) which show
 808 retreat of Taylor Glacier in Pearse Valley during MIS 5a, and the MIS 5 / 4 transition.

809

810 **5.4 Advance and retreat of outlet and alpine glaciers during interglacial periods**

811 Our new data has implications regarding the relationship between outlet and alpine glacier behaviour,
 812 regional paleoclimate, and the extent of sea ice and open ocean conditions in the Ross Sea. Snow
 813 accumulation rate, atmospheric temperature, and duration of precipitation appear to be the major
 814 controls governing the advance and retreat of Taylor Glacier during previous warm intervals (Fig. 13).
 815 In central Taylor Valley, substage 5a and 5c sediments bury 5e sediments suggesting Taylor Glacier
 816 responds to regional changes over millennial timescales (Higgins et al., 2000a). The Taylor Glacier
 817 advances in central Taylor Valley during substages 5e, 5c and 5a correspond with increased
 818 accumulation in Taylor Dome (Higgins et al., 2000a; Steig et al., 2000). Our exposure ages indicate the
 819 retreat of Taylor Glacier in Pearse Valley occurred at ~65–74 ka, during the MIS 5 / 4 transition, and is

820 consistent with the retreat in central Taylor Valley. The presence of a lobe of Taylor Glacier in Pearse
821 Valley throughout MIS 5 is likely linked to prolonged interglacial climate conditions. The interglacial-
822 mode climate, where austral westerlies are in a poleward-shifted position for prolonged periods during
823 MIS 5, is associated with periods where CO₂ concentrations were above ~230 ppm, the glacial-
824 interglacial CO₂ threshold proposed by Denton et al. (2021).

825 Yan et al. (2021) suggested that peak accumulation rates occurred at ~128 ka in Southern Victoria Land
826 and are associated with reduced sea ice and possibly retreat of the Ross Ice Shelf. The study suggested
827 by ~125 ka, the Ross Ice Shelf had returned to a configuration comparable to present day. However, a
828 reduction of sea ice may have enabled increased moisture delivery over Taylor Dome during MIS 5c
829 and 5a. As Higgins et al. (2000a) suggested, increased precipitation over Taylor Dome during MIS 5a
830 and 5c appears to have caused a subsequent readvance of Taylor Glacier. We acknowledge, this
831 hypothesis is speculative and requires further testing of temperature, and atmospheric circulation in
832 response to reduced sea ice extent and perhaps a reduction of the Ross Ice Shelf by climate models.

~~833 The duration of a warm interval which governs the extent of sea ice cover or open water in the Ross
834 Sea, may in turn, influence moisture transport and accumulation on Taylor Dome and the Antarctic
835 plateau. With temperatures predicted to be similar to the last interglacial in coming decades, on a
836 multicentennial to millennial scale, anti-phased MIS 5 feedbacks may provide important analogues for
837 future Antarctic ice loss (DeConto & Pollard, 2016; DeConto et al., 2021). While our geochronology
838 suggests retreat of Taylor Glacier in Pearse Valley occurred during the MIS 5 / 4 transition, probably
839 by a change in moisture regime and drying during MIS 5a, several uncertainties regarding advancing
840 and retreating ice and associated processes in the Dry Valleys region and Ross Sea need to be addressed:~~

~~841 • The timing of advance and retreat cycles of outlet and alpine glaciers during substages 5e, 5c
842 and 5a remain poorly constrained.~~

~~843 • The duration of warm intervals, bringing warm moist air to enable glacier advance is not well
844 understood.~~

~~845 • The paucity of data in the Ross Sea regarding sea ice, ice shelf, and open ocean conditions
846 during MIS 5 makes interpretation of the antiphase behaviour between advanced outlet and alpine
847 glaciers in the Dry Valleys region, and increased open ocean in the Ross Sea difficult to quantify.~~

848

849 **6 Conclusions**

850 We applied cosmogenic nuclide analysis to ~~surface cobbles and~~ ~3 m permafrost depth profiles in
851 Pearse and lower Wright valleys of the McMurdo Dry Valleys to determine their age of deposition,
852 permafrost processes and landscape evolution. Additionally, cCosmogenic surface exposure dating of
853 surface cobbles perched on large boulders at Pearse Valley provide reliable ages for the Taylor 2 Drift.

854 ~~and surface cobbles to determine permafrost processes, landscape evolution, and obtain the age of~~
855 ~~Taylor 2 Drift, and determine landscape evolution and associated processes in Pearse Valley.~~
856 ~~Paired ¹⁰Be and ²⁶Al depth profiles at Pearse Valley show a mixed-layer in the upper ~0.65 m of~~
857 ~~sediment since ~749 ka, and depth profile modelling for near-surface permafrost deposits to 1.65 m~~
858 ~~depth reveals a deposition age of 180⁺²⁰ / ₋₄₀ ka that predates MIS 5. The sharp reduction in ¹⁰Be~~
859 ~~concentrations at ~0.65 m depth in the Pearse Valley permafrost core, and presence of increased ice~~
860 ~~content reveals a paleosublimation unconformity, and suggests that these upper sediments have~~
861 ~~undergone active-layer cryoturbation. The near-surface sediment (including the surface mixed-layer~~
862 ~~0.02–0.65 m and permafrost at >0.65–1.65 -m depth) in central Pearse Valley has been deposited~~
863 ~~at frozen for at least ka, and perhaps ~180 ka based on our depth profile model, whereas, at >2.09 m~~
864 ~~depth the depositional age of the sediment must be earlier than ~180 ka.~~

865 ~~To compare processes of sediment evolution at Pearse Valley with a lower elevation, and more coastal~~
866 ~~environment, we also applied ¹⁰Be and ²⁶Al nuclide analysis to permafrost depth profiles at Lower~~
867 ~~Wright Valley. While the current deposition at the latter site occurred more recently (<25 ka), total~~
868 ~~exposure-burial histories from the two sites consistently show these sediment repositories have~~
869 ~~experienced multiple glacial-interglacial cycles achieved through the recycling of sediments for at least~~
870 ~~1.2 Ma.~~

871 Our ¹⁰Be and ²⁶Al derived surface exposure ages from cobbles emplaced on large boulders embedded
872 in the valley floor of Pearse Valley located ~3 km from Taylor Glacier lobe give a minimum zero
873 erosion age of ~65 to 74 ka for deposition of the thin, patchy drift, indicating that Taylor Glacier
874 retreated from Pearse Valley during MIS 5 / 4 transition. ~~Companion ¹⁰Be and ²⁶Al depth profile~~
875 ~~modelling reveals a ~180 ka deposition age for near-surface permafrost deposits to 1.65 m depth that~~
876 ~~predates MIS 5.~~ These data support antiphase behaviour between outlet and alpine glaciers in the
877 McMurdo Dry Valleys region and ice extent in the Ross Sea, and suggest a causal mechanism where
878 cold-based glacier advance and retreat is controlled by moisture availability and drying, respectively
879 due to ice retreat and expansion in the Ross Sea. Our work is consistent with geochronology from central
880 Taylor Valley, supporting advance and retreat cycles of Taylor Glacier during MIS substages 5c and 5a
881 (Higgins et al., 2000a), corresponding with increased accumulation at Taylor Dome (Steig et al. 2000).
882 ~~Our study highlights the need for better age constraints of alpine and outlet glaciers that advanced during~~
883 ~~MIS 5 in the Dry Valley region. In particular, for assessing the relationship between accumulation rate~~
884 ~~at Taylor Dome, and sea ice, ice shelf, and open ocean conditions in the Ross Sea during MIS 5.~~

885 ~~To compare processes of sediment evolution at Pearse Valley with a lower elevation, and more coastal~~
886 ~~environment, we also applied ¹⁰Be and ²⁶Al nuclide analysis to permafrost depth profiles at Lower~~
887 ~~Wright Valley. While the current deposition at the latter site occurred more recently (<25 ka), total~~
888 ~~exposure burial histories from the two sites consistently show these sediment repositories have~~

889 ~~experienced multiple glacial-interglacial cycles achieved through the recycling of sediments for at least~~
890 ~~1.2 Ma.~~

891

892 **Code availability**

893 The code used for depth profile modelling is available by request from the corresponding author.

894 **Data availability**

895 All data described in the paper are included in the Supplement.

896 **Author contributions**

897 JTHA, GSW, AA, and ND conducted the field work and sample collection. JTHA did the sample
898 preparation. DF and TF conducted the AMS measurement and analysis with assistance from KW. AJH
899 and JTHA developed the depth profile models. JTHA prepared the manuscript with contributions from
900 all authors.

901 **Competing interests**

902 The authors declare that they have no conflict of interest.

903 **Acknowledgements**

904 We thank Craig Cary, Ian McDonald, Bob Dagg and Steph Lambie for assistance in the field, Antarctica
905 New Zealand and Southern Lakes Helicopters for logistical support, and Steve Kotevski for laboratory
906 assistance. We thank Jane Andersen and Greg Balco for their valuable reviews which improved the
907 quality of the paper.

908 **Financial Support**

909 This research was supported by NZARI (RFP 2014-1), and ANSTO Portal grants 12215 and 12260 and
910 an AINSE Postgraduate Research Award. JTHA was supported by a Sir Robin Irvine Scholarship, and
911 a University of Otago departmental award. AA and ND were partially supported by the Russian
912 Antarctic Expedition. We acknowledge the financial support from the Australian Government for the
913 Centre for Accelerator Science at ANSTO through the National Collaborative Research Infrastructure
914 Strategy (NCRIS). Prepared in part by LLNL under Contract DE-AC52-07NA27344; LDRD grant 19-
915 LW-036. This is LLNL-JRNL-842669.

916

917

918 **References**

- 919 Adriaenssens, E. M., Kramer, R., Goethem, M. W. Van, Makhalanyaane, T. P., Hogg, I., & Cowan, D.
920 A. (2017). Environmental drivers of viral community composition in Antarctic soils identified
921 by viromics, 1–14. <https://doi.org/10.1186/s40168-017-0301-7>
- 922 Anderson, R. S., Repka, J. L., & Dick, G. S. (1996). Explicit treatment of inheritance in dating
923 depositional surfaces using in situ ^{10}Be and ^{26}Al . *Geology*, 24(1), 47–51.
924 [https://doi.org/10.1130/0091-7613\(1996\)024<0047:ETOIID>2.3.CO;2](https://doi.org/10.1130/0091-7613(1996)024<0047:ETOIID>2.3.CO;2)
- 925 Atkins, C. (2013). Geomorphological evidence of cold-based glacier activity in South Victoria Land,
926 Antarctica. *Geological Society, London, Special Publications*. <https://doi.org/10.1144/SP381.18>
- 927 Balco, G, Stone, J. O., Lifton, N. A., & Dunai, T. J. (2008). A complete and easily accessible means
928 of calculating surface exposure ages or erosion rates from ^{10}Be and ^{26}Al measurements.
929 *Quaternary Geochronology*, 3(3), 174–195. <https://doi.org/10.1016/j.quageo.2007.12.001>
- 930 Balco, G. (2017). Production rate calculations for cosmic-ray-muon-produced ^{10}Be and ^{26}Al
931 benchmarked against geological calibration data. *Quaternary Geochronology*, 39, 150–173.
932 <https://doi.org/10.1016/j.quageo.2017.02.001>
- 933 Bergelin, M., Putkonen, J., Balco, G., Morgan, D., Corbett, L. B., & Bierman, P. R. (2022).
934 Cosmogenic nuclide dating of two stacked ice masses : Ong Valley, Antarctica. *The*
935 *Cryosphere*, 16(7), 2793-2817. <https://doi.org/10.5194/tc-16-2793-2022>
- 936 Bibby, T., Putkonen, J., Morgan, D., Balco, G., & Shuster, D. L. (2016). Million year old ice found
937 under meter thick debris layer in Antarctica. *Geophysical Research Letters*, 43(13), 6995–7001.
938 <https://doi.org/10.1002/2016GL069889>
- 939 Blackburn, T., Edwards, G. H., Tulaczyk, S., Scudder, M., Piccione, G., Hallet, B., McLean, N.,
940 Zachos, J.C., Cheney, B., & Babbe, J. T. (2020). Ice retreat in Wilkes Basin of East Antarctica
941 during a warm interglacial. *Nature*, 583(7817), 554–559. [https://doi.org/10.1038/s41586-020-](https://doi.org/10.1038/s41586-020-2484-5)
942 2484-5
- 943 Bockheim, JG; Campbell, I.G., McCleod, M. (2007). Permafrost Distribution and Active-Layer
944 Depths in the McMurdo Dry Valleys, Antarctica. *Permafrost and Periglac. Process.*, 18(3),
945 217–227. <https://doi.org/10.1002/ppp.588>
- 946 Bockheim, A. J. G., Prentice, M. L., & Mcleod, M. (2008). Distribution of Glacial Deposits, Soils,
947 and Permafrost in Taylor Valley, Antarctica. *Arctic, Antarctic, and Alpine Research*, 40(2), 279–
948 286. [https://doi.org/10.1657/1523-0430\(06-057\)](https://doi.org/10.1657/1523-0430(06-057))
- 949 Borchers, B., Marrero, S., Balco, G., Caffee, M., Goehring, B., Lifton, N., Nishiizumi, K., Phillips, F.,
950 Schaefer, J., & Stone, J. (2016). Geological calibration of spallation production rates in the
951 CRONUS-Earth project. *Quaternary Geochronology*, 31, 188–198.
952 <https://doi.org/10.1016/j.quageo.2015.01.009>
- 953 Brook, E. J., Kurz, M. D., Ackert, R. P., Denton, G. H., Brown, E. T., Raisbeck, G. M., & Yiou, F.
954 (1993). Chronology of Taylor Glacier advances in Arena Valley, Antarctica, using in situ
955 cosmogenic ^3He and ^{10}Be . *Quaternary Research*, 39(1), 11-23.
956 <https://doi.org/10.1006/qres.1993.1002>
- 957 Child, D., Elliott, G., Mifsud, C., Smith, A. M., & Fink, D. (2000). Sample processing for earth
958 science studies at ANTARES. *Nuclear Instruments and Methods in Physics Research, Section*
959 *B: Beam Interactions with Materials and Atoms*, 172(1–4), 856–860.
960 [https://doi.org/10.1016/S0168-583X\(00\)00198-1](https://doi.org/10.1016/S0168-583X(00)00198-1)
- 961 Chorley, H., Levy, R., Naish, T., Lewis, A., Cox, S., Hemming, S., Ohneiser C, Gorman A, Harper M,
962 Homes A, Hopkins J., Prebble, J., Verret, M., Dickinson, W., Florindo, F., Golledge, N.,
963 Halberstadt, A. R., Kowalewski, D., McKay, R., Meyers, S., Anderson, J., Dagg, B., & Lurcock,
964 P. (2022). East Antarctic Ice Sheet variability during the middle Miocene Climate Transition

- 965 captured in drill cores from the Friis Hills, Transantarctic Mountains. *GSA Bulletin*.
966 <https://doi.org/10.1130/B36531.1>
- 967 Cook, C. P., Van De Fliedrt, T., Williams, T., *et al.* (2013). Dynamic behaviour of the East Antarctic
968 ice sheet during Pliocene warmth. *Nature Geoscience*, 6(9), 765–769.
969 <https://doi.org/10.1038/ngeo1889>
- 970 Cox, S. C., Turnbull, I. M., Isaac, M. J., Townsend, D. B., & Smith Lyttle, B. (2012). *Geology of*
971 *Southern Victoria Land, Antarctica. Institute of geological & Nuclear Sciences 1:25,000*
972 *geological map 22. 135 p. + 1 folded map.* Lower Hutt, New Zealand. GNS Science.
- 973 Davis, T. N. (2001). *Permafrost: A Guide to Frozen Ground in Transition*. Fairbanks, AK: University
974 of Alaska Press. 351 pp. ISBN 1-889963-19-4. *Journal of Glaciology*, 48(162), 478-478.
975 <https://doi.org/10.3189/172756502781831223>
- 976 DeConto, R. M., & Pollard, D. (2016). Contribution of Antarctica to past and future sea-level rise.
977 *Nature*, 531(7596), 591–597. <https://doi.org/10.1038/nature17145>
- 978 Denton, G.H., Armstrong R.L, Stuiver, M. (1970). Late Cenozoic Glaciation in Antarctica: The
979 Record in the McMurdo Sound Region. *Antarctic Journal of the United States*, 5(1), 15–21.
- 980 Denton, G. H., Putnam, A. E., Russell, J. L., Barrell, D. J. A., Schaefer, J. M., Kaplan, M. R., &
981 Strand, P. D. (2021). The Zealandia Switch: Ice age climate shifts viewed from Southern
982 Hemisphere moraines. *Quaternary Science Reviews*, 257, 106771.
983 <https://doi.org/10.1016/j.quascirev.2020.106771>
- 984 Doran, P. T., McKay, C. P., Clow, G. D., Dana, G. L., Fountain, A. G., Nysten, T., & Lyons, W. B.
985 (2002). Valley floor climate observations from the McMurdo dry valleys, Antarctica, 1986-
986 2000. *Journal of Geophysical Research Atmospheres*, 107(24), ACL 13-1-ACL 13-12.
987 <https://doi.org/10.1029/2001JD002045>
- 988 Dutton, A., Carlson, A. E., Long, A. J., Milne, G. A., Clark, P. U., DeConto, R., Horton, B.,
989 Rahmstorf, S., & Raymo, M. E. (2015). Sea-level rise due to polar ice-sheet mass loss during
990 past warm periods. *Science*, 349(6244). <https://doi.org/10.1126/science.aaa4019>
- 991 Dutton, A., & Lambeck, K. (2012). Ice volume and sea level during the last interglacial. *Science*,
992 337(6091), 216–219. <https://doi.org/10.1126/science.1205749>
- 993 Fink, D., Augustinus, P., Rhodes, E., Bristow, C., & Balco, G. (2015). ²¹Ne, ¹⁰Be and ²⁶Al
994 cosmogenic burial ages of near-surface eolian sand from the Packard Dune field, McMurdo Dry
995 Valleys, Antarctica. *EGU General Assembly Vol. 17. 2015EGUGA..17.2922F*
- 996 Fischer, H., Meissner, K. J., Mix, A. C., Abram, N. J., Austermann, J., Brovkin, V., *et al.* (2018).
997 Palaeoclimate constraints on the impact of 2 °C anthropogenic warming and beyond. *Nature*
998 *Geoscience*, 11(7), 474–485. <https://doi.org/10.1038/s41561-018-0146-0>
- 999 Fountain, A. G., Nysten, T. H., Monaghan, A., Basagic, H. J., & Bromwich, D. (2010). Snow in the
1000 Mcmurdo Dry Valleys, Antarctica. *International Journal of Climatology*, 30(5), 633–642.
1001 <https://doi.org/10.1002/joc.1933>
- 1002 French, H. M. (2017). *The periglacial environment. Wiley-Blackwell* (4th ed.). John Wiley & Sons.
- 1003 Gilichinsky, D. A., Wilson, G. S., Friedmann, E. I., McKay, C. P., Sletten, R. S., Rivkina, E. M.,
1004 Vishnivetskaya, T. A., Erokhina, L. G., Ivanushkina, N. E., Kochkina, G. A., Shcherbakova, V.
1005 A., Soina, V. S., Spirina, E. V., Vorobyova, E. A., Fyodorov-Davydov, D. G., Hallet, B.,
1006 Ozerskaya, S. M., Sorokovikov, V. A., Laurinavichyus, K. S., Shatilovich, A. V., Chanton, J. P.,
1007 Ostroumov, V. E., & Tiedje, J. M. (2007). Microbial populations in Antarctic permafrost:
1008 Biodiversity, stage, age, and implication for astrobiology. *Astrobiology*, 7(2), 275–311.
1009 <https://doi.org/10.1089/ast.2006.0012>

- 1010 Golledge, N. R., Clark, P. U., He, F., Dutton, A., Turney, C. S. M., Fogwill, C. J., Naish, T.R., Levy,
1011 R.H., McKay, R.M., Lowry, D.P., Bertler, N.A., Dunbar, G. B., & Carlson, A. E. (2021). Retreat
1012 of the Antarctic Ice Sheet During the Last Interglaciation and Implications for Future Change.
1013 *Geophysical Research Letters*, 48(17), 1–11. <https://doi.org/10.1029/2021GL094513>
- 1014 Gunn, B. M., & Warren, G. (1962). *Geology of Victoria Land between the Mawson and Mulock*
1015 *Glaciers, Antarctica*. New Zealand Dept. of Scientific and Industrial Research.
- 1016 Hall, B. L., Denton, G. H., & Overturf, B. (2001). Glacial Lake Wright, a high-level Antarctic lake
1017 during the LGM and early Holocene. *Antarctic Science*, 13(1), 53–60.
1018 <https://doi.org/10.1017/S0954102001000086>
- 1019 Hall, B. L., & Denton, G. H. (2005). Surficial geology and geomorphology of eastern and central
1020 Wright Valley, Antarctica. *Geomorphology*, 64(1–2), 25–65.
1021 <https://doi.org/10.1016/j.geomorph.2004.05.002>
- 1022 Heldmann, J. L., Marinova, M., Williams, K. E., Lacelle, D., McKay, C. P., Davila, A., Pollard, W.,
1023 & Andersen, D. T. (2012). Formation and evolution of buried snowpack deposits in Pearse
1024 Valley, Antarctica, and implications for Mars. *Antarctic Science*, 24(3), 299–316.
1025 <https://doi.org/10.1017/S0954102011000903>
- 1026 Hidy, A. J., Gosse, J. C., Pederson, J. L., Mattern, J. P., & Finkel, R. C. (2010). A geologically
1027 constrained Monte Carlo approach to modeling exposure ages from profiles of cosmogenic
1028 nuclides: An example from Lees Ferry, Arizona. *Geochemistry, Geophysics, Geosystems*, 11(9).
1029 <https://doi.org/10.1029/2010GC003084>
- 1030 Hidy, A. J., Gosse, J. C., Sanborn, P., & Froese, D. G. (2018). Age-erosion constraints on an Early
1031 Pleistocene paleosol in Yukon, Canada, with profiles of ¹⁰Be and ²⁶Al: Evidence for a significant
1032 loess cover effect on cosmogenic nuclide production rates. *Catena*, 165, 260–271.
1033 <https://doi.org/10.1016/j.catena.2018.02.009>
- 1034 Higgins, S. M., Denton, G. H., & Hendy, C. H. (2000b). Glacial Geomorphology of Bonney Drift,
1035 Taylor Valley, Antarctica. *Geografiska Annaler, Series A: Physical Geography*, 82A(2&3), 365–
1036 389. <https://doi.org/10.1111/1468-0459.00129>
- 1037 Higgins, S. M., Hendy, C. H., & Denton, G. H. (2000a). Geochronology of Bonney Drift, Taylor
1038 Valley, Antarctica: Evidence for interglacial expansions of Taylor Glacier. *Geografiska Annaler,*
1039 *Series A: Physical Geography*, 82(2–3), 391–409. [https://doi.org/10.1111/j.0435-](https://doi.org/10.1111/j.0435-3676.2000.00130.x)
1040 [3676.2000.00130.x](https://doi.org/10.1111/j.0435-3676.2000.00130.x)
- 1041 Hrbáček, F., Oliva, M., Hansen, C., Balks, M., O’Neill, T. A., de Pablo, M. A., Ponti, S., Ramos, M.,
1042 Vieira, G., Abramov, A., Pastříková, L. K., Guglielmin, M., Goyanes, G., Francelino, M. R.,
1043 Schaefer, C., & Lacelle, D. (2023). Active layer and permafrost thermal regimes in the ice-free
1044 areas of Antarctica. *Earth-Science Reviews*, 242(October 2022).
1045 <https://doi.org/10.1016/j.earscirev.2023.104458>
- 1046 IPCC. (2021). Climate Change 2021. *The Physical Science Basis. Contribution of Working Group 1*
1047 *to Sixth Assessment Report of the Intergovernmental Panel on Climate Change*, In Press.
1048 Retrieved from <https://www.ipcc.ch/report/ar6/wg1/>
- 1049 Jouzel, J., Masson-Delmotte, V., & Cattani, O, Dreyfus G, Falourd S, Hoffmann G, Minster B, Nouet
1050 J, Barnola JM, Chappellaz J, Fischer H., *et al.* (2007). Orbital and millennial Antarctic climate
1051 variability over the past 800,000 years. *Science*, 317(5839), 793-796.
1052 <http://doi.org/10.1126/science.11410>
- 1053 Joy, K., Fink, D., Storey, B., De Pascale, G. P., Quigley, M., & Fujioka, T. (2017). Cosmogenic
1054 evidence for limited local LGM glacial expansion, Denton Hills, Antarctica. *Quaternary Science*
1055 *Reviews*, 178, 89–101. <https://doi.org/10.1016/j.quascirev.2017.11.002>

- 1056 Knudsen, M. F., Egholm, D. L., & Jansen, J. D. (2019). Quaternary Geochronology Time-integrating
1057 cosmogenic nuclide inventories under the influence of variable erosion, exposure, and sediment
1058 mixing. *Quaternary Geochronology*, 51, 110–119. <https://doi.org/10.1016/j.quageo.2019.02.005>
- 1059 Kopp, R. E., Simons, F. J., Mitrovica, J. X., Maloof, A. C., & Oppenheimer, M. (2009). Probabilistic
1060 assessment of sea level during the last interglacial stage. *Nature*, 462(7275), 863–867.
1061 <https://doi.org/10.1038/nature08686>
- 1062 Lal, D., & Chen, J. (2005). Cosmic ray labeling of erosion surfaces II: Special cases of exposure
1063 histories of boulders, soils and beach terraces. *Earth and Planetary Science Letters*, 236, 797–
1064 813. <https://doi.org/10.1016/j.epsl.2005.05.025>
- 1065 Lapalme, C. M., Lacelle, D., Pollard, W., Fortier, D., Davila, A., & McKay, C. P. (2017).
1066 Cryostratigraphy and the Sublimation Unconformity in Permafrost from an Ultraxerous
1067 Environment, University Valley, McMurdo Dry Valleys of Antarctica. *Permafrost and*
1068 *Periglacial Processes*, 28(4), 649–662. <https://doi.org/10.1002/ppp.1948>
- 1069 Lee, J. E., Brook, E. J., Bertler, N. A. N., Buizert, C., Baisden, T., Blunier, T., Ciobanu, V. G.,
1070 Conway, H., Dahl-Jensen, D., Fudge, T. J., Hindmarsh, R., Keller, E. D., Parrenin, F.,
1071 Severinghaus, J. P., Vallelonga, P., Waddington, E. D., & Winstrup, M. (2020). An 83 000-year-
1072 old ice core from Roosevelt Island, Ross Sea, Antarctica. *Climate of the Past*, 16(5), 1691–1713.
1073 <https://doi.org/10.5194/cp-16-1691-2020>
- 1074 Lewis, A. R., & Ashworth, A. C. (2016). An early to middle Miocene record of ice-sheet and
1075 landscape evolution from the Friis Hills, Antarctica. *Geological Society of America Bulletin*,
1076 128(5–6), 719–738. <https://doi.org/10.1130/b31319.1>
- 1077 Lifton, N., Sato, T., & Dunai, T. J. (2014). Scaling in situ cosmogenic nuclide production rates using
1078 analytical approximations to atmospheric cosmic-ray fluxes. *Earth and Planetary Science*
1079 *Letters*, 386, 149–160. <https://doi.org/10.1016/j.epsl.2013.10.052>
- 1080 Marchant, D. R., Denton, G. H., Bockheim, J. G., Wilson, S. C., & Kerr, A. R. (1994). Quaternary
1081 changes in level of the upper Taylor Glacier, Antarctica: implications for paleoclimate and East
1082 Antarctic Ice Sheet dynamics. *Boreas*, 23(1), 29–43. <https://doi.org/10.1111/j.1502-3885.1994.tb00583.x>
- 1084 Marchant, D. R., & Denton, G. H. (1996). Miocene and Pliocene paleoclimate of the Dry Valleys
1085 region, Southern Victoria land: A geomorphological approach. *Marine Micropaleontology*,
1086 27(1–4), 253–271. [https://doi.org/10.1016/0377-8398\(95\)00065-8](https://doi.org/10.1016/0377-8398(95)00065-8)
- 1087 Marchant, D. R., & Head, J. W. (2007). Antarctic dry valleys: Microclimate zonation, variable
1088 geomorphic processes, and implications for assessing climate change on Mars. *Icarus*, 192(1),
1089 187–222. <https://doi.org/10.1016/j.icarus.2007.06.018>
- 1090 Marchant, D. R., Mackay, S. L., Lamp, J. L., Hayden, A. T., & Head, J. W. (2013). A review of
1091 geomorphic processes and landforms in the Dry Valleys of southern Victoria Land: Implications
1092 for evaluating climate change and ice-sheet stability. *Geological Society Special Publication*,
1093 381(1), 319–352. <https://doi.org/10.1144/SP381.10>
- 1094 Marrero, S. M., Hein, A. S., Naylor, M., Attal, M., Shanks, R., Winter, K., Woodward, J., Dunning,
1095 S., Westoby, M., & Sugden, D. (2018). Controls on subaerial erosion rates in Antarctica. *Earth*
1096 *and Planetary Science Letters*, 501, 56–66. <https://doi.org/10.1016/j.epsl.2018.08.018>
- 1097 Mercader, J., Gosse, J. C., Bennett, T., Hidy, A. J., & Rood, D. H. (2012). Cosmogenic nuclide age
1098 constraints on Middle Stone Age lithics from Niassa, Mozambique. *Quaternary Science*
1099 *Reviews*, 47, 116–130. <https://doi.org/10.1016/j.quascirev.2012.05.018>
- 1100 Mifsud, C., Fujioka, T., & Fink, D. (2013). Extraction and purification of quartz in rock using hot
1101 phosphoric acid for in situ cosmogenic exposure dating. *Nuclear Instruments and Methods in*

- 1102 *Physics Research Section B: Beam Interactions with Materials and Atoms*, 294, 203–207.
1103 <https://doi.org/10.1016/j.nimb.2012.08.037>
- 1104 Morgan, D. J., Putkonen, J., Balco, G., & Stone, J. (2011). Degradation of glacial deposits quantified
1105 with cosmogenic nuclides, Quartermain Mountains, Antarctica. *Earth Surface Processes and*
1106 *Landforms*, 36(2), 217–228. <https://doi.org/10.1002/esp.2039>
- 1107 Morgan, D., Putkonen, J., Balco, G., & Stone, J. (2010). Quantifying regolith erosion rates with
1108 cosmogenic nuclides ^{10}Be and ^{26}Al in the McMurdo Dry Valleys, Antarctica. *Journal of*
1109 *Geophysical Research: Earth Surface*, 115(3), 1–17. <https://doi.org/10.1029/2009JF001443>
- 1110 Naish, T., Powell, R., Levy, R., Wilson, G., Scherer, R., Talarico, F., *et al.* (2009). Obliquity-paced
1111 Pliocene West Antarctic ice sheet oscillations. *Nature*, 458(7236), 322–328.
1112 <https://doi.org/10.1038/nature07867>
- 1113 Ng, F., Hallet, B., Sletten, R. S., & Stone, J. O. (2005). Fast-growing till over ancient ice in Beacon
1114 Valley, Antarctica. *Geology*, 33(2), 121–124. <https://doi.org/10.1130/G21064.1>
- 1115 Nishiizumi, K. (2004). Preparation of ^{26}Al AMS standards. *Nuclear Instruments and Methods in*
1116 *Physics Research Section B: Beam Interactions with Materials and Atoms*, 223–224, 388–392.
1117 <https://doi.org/10.1016/j.nimb.2004.04.075>
- 1118 Nishiizumi, K., Imamura, M., Caffee, M. W., Southon, J. R., Finkel, R. C., & McAninch, J. (2007).
1119 Absolute calibration of ^{10}Be AMS standards. *Nuclear Instruments and Methods in Physics*
1120 *Research Section B: Beam Interactions with Materials and Atoms*, 258(2), 403–413.
1121 <https://doi.org/10.1016/j.nimb.2007.01.297>
- 1122 Otto-Bliesner, B. L., Rosenbloom, N., Stone, E. J., McKay, N. P., Lunt, D. J., Brady, E. C., &
1123 Overpeck, J. T. (2013). How warm was the last interglacial? new model-data comparisons.
1124 *Philosophical Transactions of the Royal Society A: Mathematical, Physical and Engineering*
1125 *Sciences*, 371(2001). <https://doi.org/10.1098/rsta.2013.0097>
- 1126 Patterson, M. O., McKay, R., Naish, T., Escutia, C., Jimenez-Espejo, F. J., Raymo, M. E., Meyers, S.
1127 R., Tauxe, L., Brinkhuis, H., & IODP Expedition 318 Scientists (2014). Orbital forcing of the
1128 East Antarctic ice sheet during the Pliocene and Early Pleistocene. *Nature Geoscience*, 7(11),
1129 841–847. <https://doi.org/10.1038/ngeo2273>
- 1130 Pollard, D., & DeConto, R. M. (2009). Modelling West Antarctic ice sheet growth and collapse
1131 through the past five million years. *Nature*, 458(7236), 329–332.
1132 <https://doi.org/10.1038/nature07809>
- 1133 Putkonen, J., Balco, G., & Morgan, D. (2008). Slow regolith degradation without creep determined by
1134 cosmogenic nuclide measurements in Arena Valley, Antarctica. *Quaternary Research*, 69(2),
1135 242–249. <https://doi.org/10.1016/j.yqres.2007.12.004>
- 1136 Ruggiero, L., Sciarra, A., Mazzini, A., Florindo, F., Wilson, G., Tartarello, M. C., Mazzoli, C.,
1137 Anderson, J. T. H., Romano, V., Worthington, R., Bigi, S., Sassi, R., & Ciotoli, G. (2023).
1138 Antarctic permafrost degassing in Taylor Valley by extensive soil gas investigation. *Science of*
1139 *the Total Environment*, 866, 161345. <https://doi.org/10.1016/j.scitotenv.2022.161345>
- 1140 Salvatore, M. R., & Levy, J. S. (2021). *Chapter 11: The McMurdo Dry Valleys of Antarctica: a*
1141 *geological environment and ecological analog to the Martian surface and near surface. Mars*
1142 *Geological Enigmas*. Elsevier Inc. 291–332 [https://doi.org/10.1016/B978-0-12-820245-6/00011-](https://doi.org/10.1016/B978-0-12-820245-6/00011-2)
1143 [2](https://doi.org/10.1016/B978-0-12-820245-6/00011-2)
- 1144 Schäfer, J. M., Baur, H., Denton, G. H., Ivy-Ochs, S., Marchant, D. R., Schlüchter, C., & Wieler, R.
1145 (2000). The oldest ice on Earth in Beacon Valley, Antarctica: New evidence from surface
1146 exposure dating. *Earth and Planetary Science Letters*, 179(1), 91–99.
1147 [https://doi.org/10.1016/S0012-821X\(00\)00095-9](https://doi.org/10.1016/S0012-821X(00)00095-9)

- 1148 Steig, E. J., Morse, D. L., Waddington, E. D., Stuiver, M., Pieter, M., Mayewski, P. A., Twickler,
1149 M.S., & Whitlow, S.I. (2000). Wisconsinan and Holocene climate history from an ice core at
1150 Taylor Dome , western Ross Embayment , Antarctica. *Geografiska Annaler: Series A, Physical*
1151 *Geography*, 82(2-3), pp.213-235. <https://doi.org/10.1111/j.0435-3676.2000.00122.x>
- 1152 Sugden, D. E., Marchant, D. R., Potter, N., Souchez, R. A., Denton, G. H., Swisher, C. C., & Tison, J.
1153 L. (1995). Preservation of Miocene glacier ice in East Antarctica. *Nature*, 376(6539), 412–414.
1154 <https://doi.org/10.1038/376412a0>
- 1155 Summerfield, M. A., Sugden, D. E., Denton, G. H., Marchant, D. R., Cockburn, H. A. P., & Stuart, F.
1156 M. (1999). Cosmogenic isotope data support previous evidence of extremely low rates of
1157 denudation in the Dry Valleys region, southern Victoria Land, Antarctica. *Geological Society*
1158 *Special Publication*, 162, 255–267. <https://doi.org/10.1144/GSL.SP.1999.162.01.20>
- 1159 Sutter, J., Eisen, O., Werner, M., Grosfeld, K., Kleiner, T., & Fischer, H. (2020). Limited Retreat of
1160 the Wilkes Basin Ice Sheet During the Last Interglacial. *Geophysical Research Letters*, 47(13).
1161 <https://doi.org/10.1029/2020GL088131>
- 1162 Swanger, K. M., Babcock, E., Winsor, K., & Valletta, R. D. (2019). Rock glaciers in Pearse Valley,
1163 Antarctica record outlet and alpine glacier advance from MIS 5 through the Holocene.
1164 *Geomorphology*, 336, 40–51. <https://doi.org/10.1016/j.geomorph.2019.03.019>
- 1165 Swanger, K. M., Lamp, J. L., Winckler, G., Schaefer, J. M., & Marchant, D. R. (2017). Glacier
1166 advance during Marine Isotope Stage 11 in the McMurdo Dry Valleys of Antarctica. *Scientific*
1167 *Reports*, 7, 1–9. <https://doi.org/10.1038/srep41433>
- 1168 Swanger, K. M., Marchant, D. R., Schaefer, J. M., Winckler, G., & Head, J. W. (2011). Elevated East
1169 Antarctic outlet glaciers during warmer-than-present climates in southern Victoria Land. *Global*
1170 *and Planetary Change*, 79(1–2), 61–72. <https://doi.org/10.1016/j.gloplacha.2011.07.012>
- 1171 Turney, C. S. M., Fogwill, C. J., Golledge, N. R., McKay, N. P., van Sebille, E., Jones, R. T.,
1172 Etheridge, D., Rubino, M., Thornton, D. P., Davies, S. M. and Ramsey, C. B., *et al.* (2020).
1173 Early Last Interglacial ocean warming drove substantial ice mass loss from Antarctica.
1174 *Proceedings of the National Academy of Sciences of the United States of America*, 117(8), 3996–
1175 4006. <https://doi.org/10.1073/pnas.1902469117>
- 1176 Wilcken, K. M., Fujioka, T., Fink, D., Fülöp, R. H., Codilean, A. T., Simon, K., Mifsud, C., &
1177 Kotevski, S. (2019). SIRIUS Performance: ¹⁰Be, ²⁶Al and ³⁶Cl measurements at ANSTO.
1178 *Nuclear Instruments and Methods in Physics Research, Section B: Beam Interactions with*
1179 *Materials and Atoms*, 455, 300–304. <https://doi.org/10.1016/j.nimb.2019.02.009>
- 1180 Wilson, D. J., Bertram, R. A., Needham, E. F., Flierdt, T. Van De, Welsh, K. J., Mckay, R. M.,
1181 Mazumder, A., Riesselman, C.R., Jimenez-Espejo, F.J., & Escutia, C. (2018). Ice loss from the
1182 East Antarctic Ice Sheet during late Pleistocene interglacials. *Nature*, 561(7723), 383–386.
1183 <https://doi.org/10.1038/s41586-018-0501-8>
- 1184 Yan, Y., Spaulding, N. E., Bender, M. L., Brook, E. J., Higgins, J. A., Kurbatov, A. V., & Mayewski,
1185 P. A. (2021). Enhanced Moisture Delivery into Victoria Land , East Antarctica During the Early
1186 Last Interglacial: implications for West Antarctic Ice Sheet Stability. *Climate of the Past*, 17(5),
1187 1841-1855. <https://doi.org/10.5194/cp-17-1841-2021>
- 1188 Yershov, E. D. (1998). *General Geocryology. Studies in Polar Research.* (P. J. Williams, Ed.).
1189 Cambridge: Cambridge University Press. <https://doi.org/doi:10.1017/CBO9780511564505>
- 1190
- 1191
- 1192